The Dissertation Committee for Deepa Gazula Certifies that this is the approved version of the following dissertation:

Epitaxial Regrowth based Fabrication Process for Vertical Cavity Lasers

Committee:

Dennis G. Deppe, Supervisor

Joe Campbell

Ananth Dodabalapur

Archie Holmes

Brian Korgel

Epitaxial Regrowth Based Fabrication Process for Vertical Cavity Lasers

by

Deepa Gazula, B.S., M.S.

Dissertation

Presented to the Faculty of the Graduate School of

The University of Texas at Austin

in Partial Fulfillment

of the Requirements

for the Degree of

Doctor of Philosophy

The University of Texas at Austin

December, 2006

To

My Parents

Acknowledgements

I would like to express my sincere appreciation to my advisor, Prof. Dennis Deppe for the opportunity to work in this exciting field. His keen insights and breadth of knowledge have helped me examine problems at a fundamental level and become a better researcher.

Many thanks to my committee members Prof. Campbell, Prof. Holmes, Prof. Dodabalapur, and Prof. Korgel for their time and interest in this work.

I would like to thank the present and former members of the group with whom I had many interesting and valuable discussions related to this work. They have made my stay here very memorable. Thanks are also due to the MER staff for making sure things were running smoothly in the lab all the time.

My parents have very selflessly cared all these years to bring me to where I am today. I am especially thankful to them for being there for me and believing in me all these years.

Finally, I am grateful to my husband Sreekumar for his love and support. It was a roller coaster ride pursuing graduate studies together. But his cheerfulness and optimism made it a very enjoyable one.

Epitaxial Regrowth Based Fabrication Process for Vertical Cavity Lasers

Publication No._____

Deepa Gazula, Ph.D.

The University of Texas at Austin, 2006

Supervisor: Dennis G. Deppe

GaAs based oxide confined vertical-cavity surface-emitting lasers (VCSELs) have demonstrated record performance in terms of low threshold current, high modulation speed and high wall-plug efficiency. However, oxide-confined VCSELs have reliability and non-uniformity problems that limit scaling to small active volumes for single mode operation or to micro-cavity dimensions for quantum light sources. The optical mode is also difficult to engineer since aperture geometries are limited. These limitations call for the development of a new technology that provides full control of modal overlap with optical gain, and this requires patterning of the VCSEL's transverse mode- and current-confinement. A new approach presented in this dissertation demonstrates a very important attribute in providing lithographically defined and self-aligned mode- and current-confinement suitable for arbitrary patterning and size scaling, and for high

reliability, is based on an all-epitaxial device. The fabrication process involves epitaxial regrowth over shallow mesas to incorporate these intra-cavity patterns that have direct overlap with the optical mode. These intracavity gratings are defined by lithography and a selective etching process after the first stage of epitaxial growth. In this work, a VCSEL with an intracavity grating has been realized that shows an increase in the slope efficiency due to better matching of the gain and optical mode in comparison to a device that lacks the grating. Using a similar regrowth process, a laser diode incorporating a buried high index contrast GaAs-air (etched void) photonic pattern within the cavity has also been demonstrated.

Epitaxial quantum dots (QDs) present new opportunities in semiconductor light sources due to their charge localization and modified electronic density of states. It is especially interesting to combine QDs with a microcavity VCSEL, since electronic and photonic confinement become scalable in a device that can have important commercial applications. This has been achieved in a buried heterostructure VCSEL that employs an intracavity mesa to confine the quantum dots and optical mode to the same regions in the cavity. Cavity quality factors as high as 33000 are measured, and ground state lasing is demonstrated with a single quantum dot active layer for temperatures up to 110 K.

Table of Contents

CHAPTER 1

INTRODUCTION

1.1 Trends in VCSEL Development

The vertical cavity surface emitting laser (VCSEL) has gone through an interesting progression of advances. After an extended period of research and development by Iga [1], a performance breakthrough was achieved by Jewell and his coworkers by demonstrating current injection VCSELs with epitaxial mirrors and only a few quantum wells [2]. This all-epitaxial approach led to the VCSEL's commercialization. Then, when all-epitaxial VCSELs were seemingly well-established and believed to be near optimum performance, another breakthrough, oxide-confinement [3], showed how proton-implanted or etched-pillar devices suffer from optical loss created by transverse mode-confinement. This has spurred further development, and over the past two decades GaAs-based VCSELs have emerged as one of the most attractive light sources for high speed, short distance interconnects, printing, optical switching, sensing and other applications. VCSELs provide many advantages over conventional edge emitting lasers, such as low divergence circular beam output, low threshold currents, low cost and high volume manufacturing by allowing wafer scale testing, and has the potential for obtaining two dimensional arrays and integrated modules on wafer.

In a VCSEL device, optical gain is provided by stimulated emission via electrical current injected into the active region. The optical cavity formed by highly reflective mirrors on either side of the active region provides the necessary feedback to sustain laser oscillation. In order to obtain lasing, it is important to effectively confine carriers and the optical mode into a small volume of the active region. Different electrical and optical confinement schemes have been implemented for this purpose.

A confinement solution that takes advantage of index guiding is that of etched mesa VCSELs [4] as shown in figure 1.1 (a). In these devices, deeply etched pillars provide lateral optical confinement due to the high index contrast between semiconductor and air, but this occurs at the expense of increased lateral losses due to optical scattering or surface recombination. Current is confined to the lateral dimensions of the mesa, however, carriers can diffuse laterally in the active region. Another popular scheme (figure 1.1 (b)) is gain guiding in planar, proton implanted VCSELs [5]. Proton implant can be used to selectively produce a buried current blocking layer to funnel current through a small area of the active layer to provide the desired current confinement. Optical confinement is achieved because of the gain-guiding, which gives rise to lateral index guiding due to thermal lensing effects. A major drawback is that there is no other index guiding mechanism, while another concern is to prevent implant damage to the active layer. The biggest

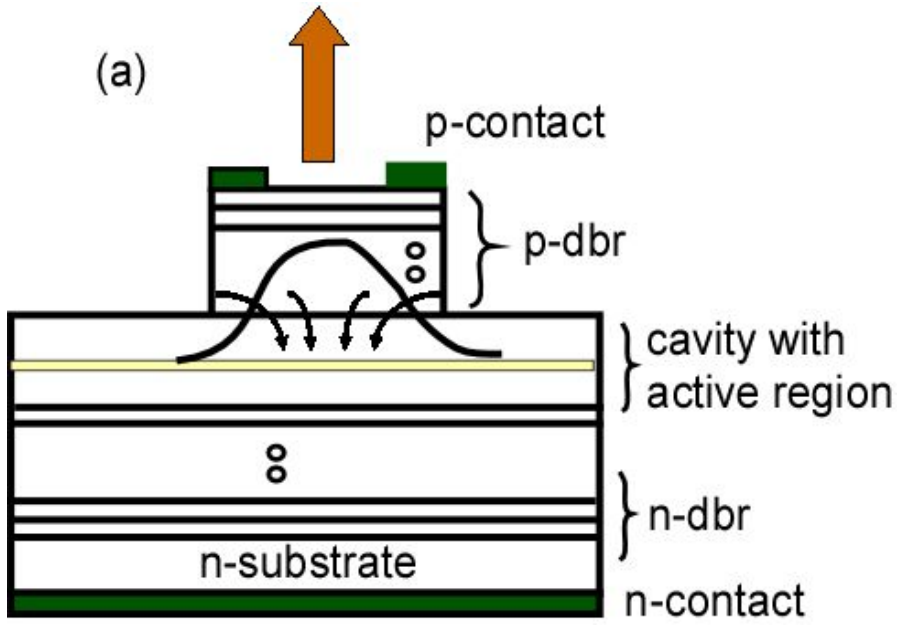
(a)
p-contact
p-dbr
cavity with
active region
n-dbr
n-substrate
n-contact

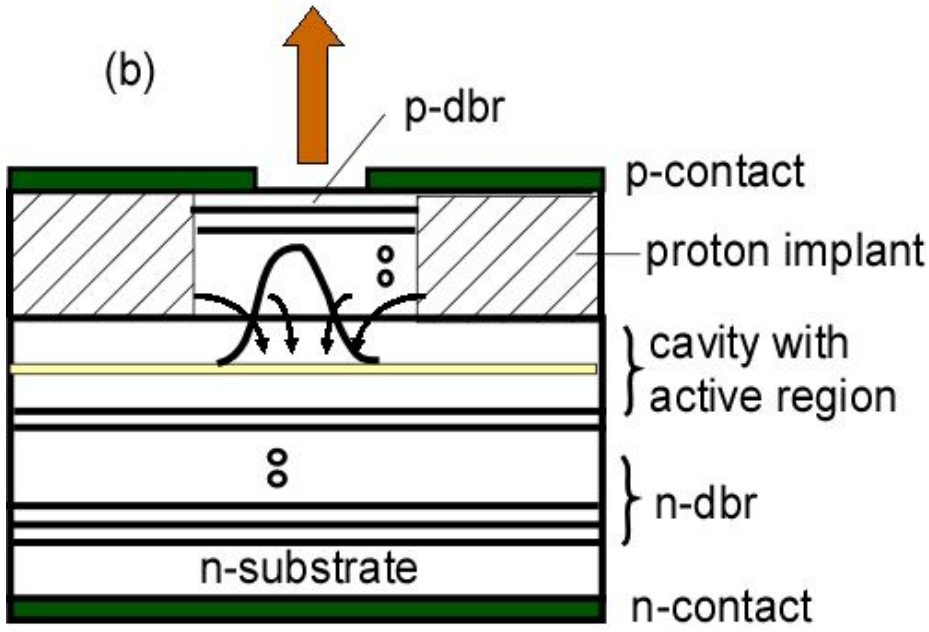
(b)
p-dbr
p-contact
proton implant
cavity with
active region
n-dbr
n-substrate
n-contact

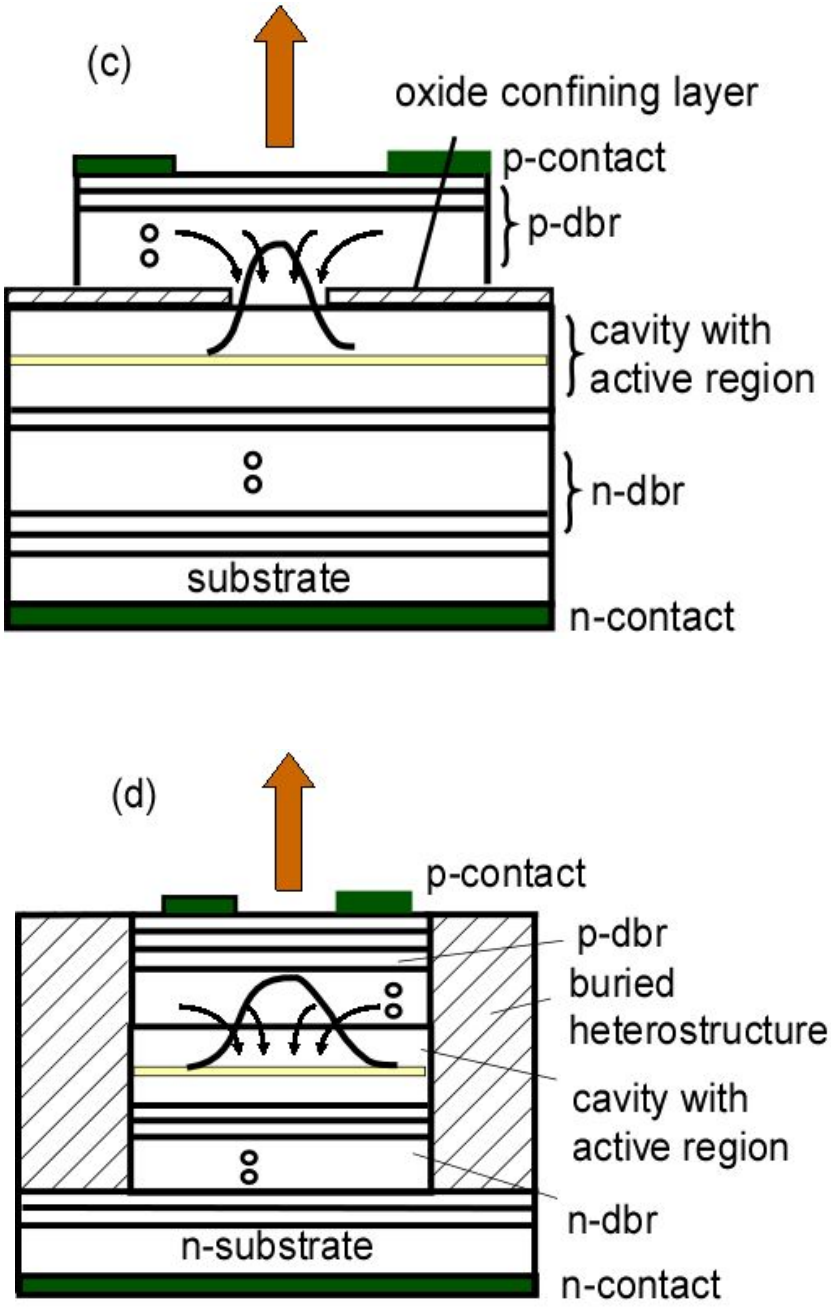

Figure 1.1: Schematic of various confinement schemes in VCSEL structures. (a) Etched post VCSEL (b) Proton implanted VCSEL (c) Oxide confined VCSEL (d) Buried heterostructure VCSEL.

advantage of this structure, however, is its planar configuration that allows a straightforward fabrication process. Most commercially available VCSELs are proton-implanted devices with multi-transverse mode behavior. The third approach seen in figure 1.1 (c) is an oxide confined VCSEL [3], where high aluminum content AlGaAs layers are subjected to a wet oxidation process to form an oxide, which is chemically inert, has high resistivity and a low refractive index [6]. The oxide layer defines an aperture through which the carriers are funneled and this provides the current confinement, while the low index provides lateral confinement through index guiding. Buried heterostructure VCSEL [7] is another kind of VCSEL structure which involves regrowth over a deeply etched mesa. This is shown in figure 1.1 (d). The regrown material surrounding the etched mesa has a lower bandgap and lower index to confine the carriers and optical mode respectively. However, it is difficult to obtain current confinement and also good quality regrowth over deep pillars that contain high aluminum composition mirror layers. Other approaches to mode- and current-confinement have been to use shallow mesas with non-epitaxial mirrors, sometimes using implantation or tunnel junctions for current-confinement [8], [9]. However, the tunnel junction/mesa approach yields an undesirable mesa step and additional voltage drop when used in GaAs based devices. In addition, dielectric mirrors can introduce material strain, complicate device fabrication, and degrade reliability.

Oxide-confined VCSELs have shown the best performance so far with respect to low threshold currents [10,11], high modulation speed [12], and high wall-plug efficiency [13]. These results may lead one to believe that oxide confinement has now taken the VCSEL to its ultimate performance. Instead, VCSELs are still limited in ways that are difficult to address with oxide confinement. Oxide formation process also has several drawbacks. The oxide layer formed by wet oxidation has a different thermal expansion coefficient than the semiconductor [3] and causes internal device strain, and can degrade reliability. Because the wet oxidation is also difficult to laterally control, small or single mode devices can suffer poor uniformity. The optical mode is also difficult to engineer since the aperture geometries are limited. While these limitations are not so serious for moderate speed (< 5 GB/s) large aperture multimode VCSELs, it is highly desirable to develop a VCSEL technology that provides scaling to small active volumes, and that allows the mode confinement to be patterned such as needed for polarization control, improved single mode output by using intracavity two-dimensional gratings or photonic crystals.

1.2 Motivation and Objectives

1.2.1 Photonic Pattern and Grating Confined Lasers

The surprising steps in VCSEL development have come mainly for two reasons. First, more so than other semiconductor lasers, the VCSEL's short gain path makes its performance very sensitive to cavity loss, and therefore sensitive to both mirror reflectivity and lateral optical loss caused by scattering or diffraction. And second, while transverse effects due to gain overlap and modal control scale with the stripe width in edge-emitting lasers, in the VCSEL they scale with its radius squared. Oxide-confinement gave a surprising solution to the lateral optical loss problem, which is to rely on resonance shifts in the otherwise planar microcavity. However, besides the reliability problems caused by its mechanical strain and its uniformity problems, oxide-confinement still does not solve the radius-squared problem of gain overlap. Even if perimeter current crowding is avoided to obtain uniform current injection, a large oxide aperture injects majority of its current around the aperture's perimeter, while the optical mode is ideally peaked at the aperture center. The result of even uniform current injection is therefore increased threshold, decreased efficiency, and spatial hole burning, each stemming from poor transverse modal overlap with the optical gain. Reducing the oxide aperture size does not solve the problem. Instead carriers diffuse outside the aperture for several microns, increasing the threshold current and parasitic capacitance, while optical loss increases.

The limitations of oxide-confinement provide motivation for pursuing a new technology that provides full control of the modal overlap with the VCSEL's optical gain. Such a control requires patterning of both the transverse mode- and current-confinement in the VCSEL. The objective of this research is to develop a new kind of vertical cavity laser diode with intra-cavity gratings and photonic crystals that can modify the transverse mode in the device. The ability to have nano-scale patterning within the optical cavity for photonic devices opens up the design space to engineer novel kinds of optical mode control. The fabrication process involves epitaxial regrowth over shallow mesas to incorporate these intra-cavity patterns in photonic devices. These gratings mesas which are intra-cavity phase shifting mesas [14] are defined by lithography and a selective etching process after the first stage of epitaxial growth which comprise of bottom distributed Bragg reflector (DBR) mirror pairs followed by the cavity spacer, active region and mesa layers. An epitaxial regrowth of semiconductor mirrors over the mesa simultaneously confines the mode in vertical and lateral directions. The placement of grating is designed such that it has direct overlap with the lasing mode. A schematic of one such laser is shown in figure 1.2. Examples of various designs of grating mesas are shown in figure 1.3. These are the top views of grating VCSEL of figure 1.2.

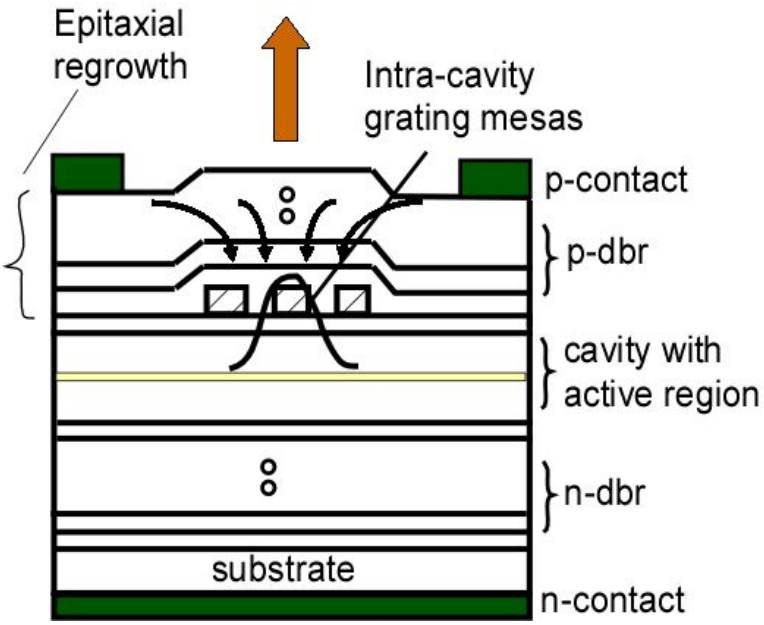

Figure 1.2: Schematic of an all-epitaxial current and mode confining VCSEL.

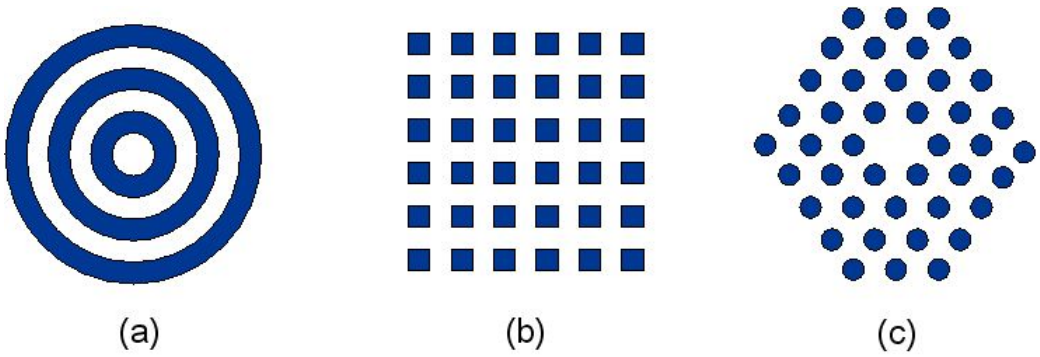

Figure 1.3: Schematic of various grating designs that can be incorporated in the grating confined VCSEL. (a) Circular grating (b) Square photonic crystal pattern (c) Photonic crystal with defect.

There has been a lot of effort in combining the cavity of the VCSEL with two dimensional (2-D) PCs. The 2-D PCs have been formed by etching holes in the crystal surface to form a periodic array, leaving an opening (defect) in the lateral PC to define the VCSEL mode [15,16]. So far though, this approach has not led to an improvement in the VCSEL characteristics. The PC does not have a strong interaction in modifying the VCSEL's optical mode, and optical scattering increases the cavity loss. In addition, single mode operation for these VCSELs requires an opening in the 2-D PC that is essentially the same size as needed in the absence of the PC, ~2 μm diameter for an 850 nm VCSEL [16]. Although this approach follows directly from the studies of 2-D PC lasers that also contain etched holes and a defect opening [17], it has the problem that low optical loss can only be achieved by keeping the interaction with the PC small through a relatively large opening in the 2-D PC. The approach with the intra-cavity PC has the potential to overcome this drawback by avoiding the use of oxide and provide low-optical loss as well as lateral mode control.

The main application for VCSELs today is for short distance multimode fiber interconnects. However, its applications could expand significantly if the single mode power could easily is increased. These include for spectroscopy, laser printing, optical storage, and in single mode fiber communication.. Highly multi-transverse mode operation, on the other hand, is required for multimode fiber interconnects in order to eliminate modal noise in the fiber. For this a relatively

large transverse mode size is needed using present designs, although the larger mode size reduces the speed and increases the threshold power of the VCSEL over what is otherwise needed. Increasing the VCSEL speed to 10 GB/sec, for example, requires a smaller device than for speeds less than 5 GB/sec. The penalty of the higher VCSEL speed achieved with a smaller transverse mode size is degradation in its multimode performance.

Although the new approach is fundamentally interesting from a basic physics standpoint, it can also greatly improve the VCSEL's performance for various applications. One of the major problems in extending the VCSEL technology to longer wavelength fiber optics has been low single mode power limited to ~1 mW because of the small required active area. This is especially true for GaAs-based VCSELs that present a low cost solution to 1.3 μm fiber optic sources, but where the power is limited by the need to achieve single mode operation. State-of-the-art single mode 1.3 μm GaAs-based VCSELs emit approximately 1 mW of power at their upper temperature of 80°C required for uncooled transceivers, while InP-based 1.3 μm distributed feedback lasers can easily emit 10 times this. Increasing the single mode VCSEL power to 10 mW would make it the laser of choice for high speed fiber interconnects. Gratings placed within the VCSEL cavity can expand this single mode area, and we believe can increase the 1.3 μm GaAs-based VCSEL powers to 5 ~ 10 mW, making them the 1.3 μm fiber optic laser of choice. Because the VCSEL's power scales as the

square of its radius, an increase in power by a factor of 10 in power requires an increase by a factor of ~3 in lateral size for single mode operation. High speed multimode VCSELs (for example for 10 GB/sec) can also be created that operate with small active areas and low threshold current to reduce overall device power, improved reliability and higher speed.

High index contrast photonic crystal (PC) patterns, which are also a type of gratings placed in a laser cavity, can also modify lateral mode propagation. Because the largest refractive index change that can be readily achieved in semiconductors is due to the semiconductor-void (air) interface, a general fabrication technique is needed that can be applied to a wide range of device structures to create photonic patterns based on such interfaces, including edge and surface emitting laser diodes. The epitaxial regrowth based process has be implemented to fabricate a laser diode with an etched void photonic crystal pattern within the cavity. In addition, the new technique allows large area 2-dimensional arrays, and could be important for very high power laser diodes that can operate at 100's of watts, with good beam characteristics and spectral control. These types of lasers are important not only for high efficiency pumping of solid-state and fiber laser devices, but also for direct laser applications in free space optical communications, as well as ladar and lidar.

1.2.2 Quantum Dot based Microcavity VCSELs

Epitaxial quantum dots (QDs) present new opportunities in semiconductor lasers and spontaneous light sources due to their charge localization and modified electronic density of states [18,19]. It is especially interesting to combine QDs with a microcavity VCSEL since electronic and photonic confinement become scalable in a device to have full electromagnetic control of light-matter interaction that can have important commercial applications. These include data communication, ultra-low power sensors, high power laser arrays, and quantum light generation. However, combining the QDs and VCSELs in a scalable fashion has been hindered by the low maximum optical gain of QD active material that requires a higher cavity quality factor (Q) than planar quantum well active material.

Planar microcavities were first used to demonstrate the Purcell effect [20] for self-organized QDs [21], and the QD spontaneous control has since been increased using etched pillar [22], oxide-apertured [23], photonic crystal defect [24] and whispering gallery mode microcavities [25]. More recently, strong coupling has been demonstrated in QD photonic crystal defect [26] and etched pillar microcavities [27]. Lasing in oxide-apertured, photonic crystal defect, and microdisk microcavities have also been demonstrated using QD ensemble active regions [28-30]. Although QD nanophotonics could lead to new technologies based on spontaneous quantum light sources and ultra-low-power, high-speed QD lasers, present semiconductor microcavities have serious drawbacks for practical

applications. Perhaps most daunting is the fragility and poor thermal conductivity that result from thin-film photonic crystals, whispering gallery microdisks, or etched pillars. Oxide confinement suffers poor controllability, making it impractical. Electrical injection in these microcavities is also difficult, if not impossible, especially because of the thin layers.

A commercial semiconductor device technology based on QD nanophotonics requires mechanically robust fabrication, excellent device thermal conductivity, lithographic control, and preferably operation at least at temperatures accessible with thermoelectric cooling (150 K). In addition, it is advantageous if the QD microcavity enables monolithic integration with electronic injection devices that can provide single-electron control. For QD lasers, a high Q (quality factor) is required to achieve threshold, while for spontaneous sources the Q needed to maximize the Purcell effect is moderate and set by the QDs spectral broadening. This calls for an approach to form a microcavity that could solve the problems that plague etched pillar, thin-film photonic crystal, and microdisk microcavities to produce a manufacturable QD microcavity source with potential for real applications. In this work, a new type of microcavity is presented that overcomes the above limitations, and it uses intracavity patterning to confine both the quantum dots and optical mode to the same regions of the cavity to obtain high Q cavities.

Lithographic definition of the photonic patterns for laser diodes and for QD microcavities provides good uniformity down to the nanometer scale, making it a

reproducible process and gives great flexibility for various grating designs. Also, all-epitaxial semiconductor devices give better reliability and thermal impedance. The fabrication process is fairly robust, and gives good yield. All these factors make it very appealing from a manufacturing perspective as well.

1.3 Thesis Outline

The work presented in this dissertation focuses on a new fabrication approach involving epitaxial regrowth over shallow mesas to introduce nanoscale intra-cavity photonic patterns such as circular gratings, photonic crystals and quantum dot based micro-cavities within GaAs based lasers.

A theoretic model is developed in chapter 2 that shows how an intra cavity grating provides mode confinement in a VCSEL. Analysis is done to understand the effect of gratings on the transverse mode characteristics. A transfer matrix formulation of Maxwell's equations for the E and H fields is used to find the eigen modes of the structure.

In Chapter 3, the fabrication procedure of an epitaxial regrowth based laser diode is described. Experimental realization of intracavity grating- and current-confined all-epitaxial VCSEL as well as a buried etched void photonic crystal based laser diode with an InGaAs/GaAs quantum well active region are explained. The technique used to obtain current confinement in the VCSEL is discussed. Also, the function of grating which is designed to match the mode and current into the

same regions of the active area to provide better overlap as well as lateral mode control is explained based on results of device characterization. Simulation of the energy band structure of the buried etched void photonic pattern in the laser cavity to determine the eigen frequencies of propagation of light is presented and the effect of photonic pattern on the laser performance is verified experimentally by comparing lasing characteristics of devices with and without the pattern.

Self-organized QDs can also be incorporated in the mode confining intra-cavity mesas to create a new type of all-epitaxial microcavity that can form a buried heterostructure VCSEL. The unique features of these devices, along with their fabrication and lasing characteristics are described in chapter 4.

Chapter 5 summarizes the work in this dissertation and concludes with directions for future research.

CHAPTER 2

THEORY AND DESIGN OF ALL-EPITAXIAL VERTICAL CAVITY LASERS

2.1 Mode confinement within the grating mesa

All-epitaxial VCSELs with intra-cavity phase shifting mesas that provide good mode confinement have been demonstrated recently [31,32]. Although oxide-confined VCSELs are often described by an effective index model [33] which shows that the effective index responsible for wave-guiding is dependent only on lateral changes in the Fabry–Perot resonance frequency, a more accurate understanding of the electromagnetic boundary conditions is required to design for low optical loss using the all-epitaxial approach. The boundary conditions that are used to model the optical mode in the mesa confined VCSELs are an extension of those given in references [34,35] as opposed to those of [33]. In this approach, the grating mesas modify the optical modes of the Fabry-perot microcavity due to the nature of electromagnetic coupling between the confined mode in the mesa region and the evanescent modes in the off-mesa regions. The placement of grating is designed such that it has direct overlap with the lasing mode. The transverse grating is created by a periodic array of cavity length changes designed to modify the laterally propagating k-vector modes. Also, the grating mesas are designed to provide simultaneous mode and current confinement within a VCSEL. It is possible

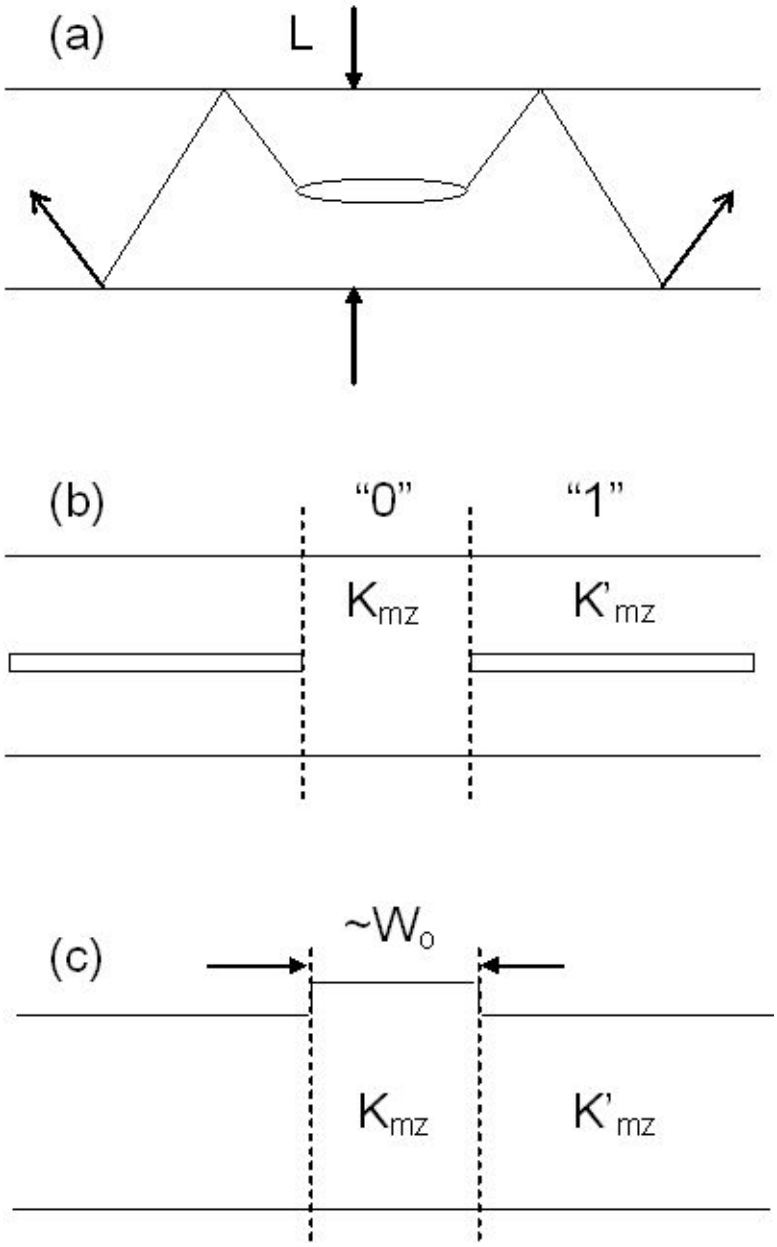

Figure 2.1: (a) A schematic illustration a planar microcavity, (b) an apertured microcavity, and (c) a mesa confined microcavity. Horizontal boundaries of the cavities (defined by L) are the reflectors, taken for argument sake as single interfaces.

to obtain reliable single mode sources, dense arrays, and also be able to repeatably control multi-mode operation.

Figure 2.1 shows schematic illustrations of various microcavities that aid in describing the all epitaxial mode confinement to be used in the grating confined VCSEL. If the cavity is planar, as shown in figure 2.1 (a), an optical mode is not confined laterally and spreads continuously due to diffraction. The lateral size of the optical mode is limited by the vertical loss rate which is set by the cavity spacer thickness and the contrast ratio (that determines the transmissivity) of the distributed Bragg reflectors. For a typical VCSEL operating at 980 nm, the lateral mode size due to this diffraction effect has a diameter of ~10 μm. In contrast, an aperture in the cavity, as shown in either figure 2.1 (b) or 2.1 (c), can laterally confine the mode and eliminate diffraction. However, the boundary condition problem of (a) is converted from a diffraction problem to a scattering problem. In figure 2.1 (b), which is similar to the now prevalent oxide-apertured VCSEL, a wave traveling laterally from region "0" in the cavity containing the lasing mode to a confining region "1" is partially reflected back into the lasing mode region and partially transmitted. To totally eliminate lateral loss we desire this lateral reflection coefficient to be unity, which is impossible to achieve perfectly in this type of cavity. However, when the cavity is very short, the reflection back into the cavity can be sufficiently close to unity to make lateral loss negligible when compared with the vertical loss due to transmission through the mirrors.

The Fabry-Perot microcavity formed by highly reflecting mirrors in figure 2.1 (c) consists of two regions with two different cavity lengths. Regions with the grating mesas and regions outside the mesas have different step heights. This gives rise to two cavity lengths that are tuned for two specific resonant wavelengths, which creates a phase shift for the resonant modes in the two regions. The region "0" is the mesa region with the longer cavity length and where the lasing eigenmode exists, while region "1" is the off-mesa region.

The optical field in the VCSEL cavity can be reasonably well described by quasi-scalar fields that satisfy the wave equation, which is given by

$$\nabla^2 E(r,\phi,z) + k_0{}^2 \varepsilon_r E(r,\phi,z) = 0 \tag{2.1}$$

where,

$$k_o = \omega\sqrt{\mu\varepsilon_o} \tag{2.2}$$

Here E represents the z component of the electric field, ω is the frequency of the field, μ is permeability of the medium, ε_o and ε_r are the permittivity of free space and the medium respectively. For a modal representation, the m^{th} mode can be described in cylindrical coordinates assuming circular symmetry for the main mode, as transverse and vertical components,

$$E_m(r,\phi,z) = E_m(r,\phi)\exp(\pm jk_z z) \tag{2.3}$$

while the cavity resonance satisfies the condition

$$k_z = \frac{m_z \pi}{L} \tag{2.4}$$

where k_z is the vertical wave vector, m_z is integer 0,1,2,… and L is the effective cavity length.

The electromagnetic boundary conditions of the cavities of figures 2.1 (b) and (c) set the frequency of the field in region "1" equal to the lasing mode of the field in region "0". This condition of equal frequency establishes the relationships between the vertical and transverse wavevector components in the two different regions. Note that for a high Q cavity, as with a VCSEL, the vertical wavevector components k_{m_z} and $k_{m'_z}$ are fixed by the cavity length and phase shift from the mirrors. For a single aperture, the lowest order mode confined in region "0" gives this relationship between the wavevectors in regions "0" and "1" by

$$\frac{\omega_o}{c} = \sqrt{\frac{(4.81)^2}{\varepsilon_r W_o^2} + k_{m_z}^2} = \sqrt{k_{m'_r}^2 + k_{m'_z}^2} \tag{2.5}$$

where W_o is the lateral size of the mode confined in region "0", and $k_{m'_r}$ is the transverse wavevector component of the field in region "1". When the cavity conditions are such that $k_{m'_z}^2 > k_{m_z}^2$ there is a range of mode sizes W_o for which $k_{m'_r}^2 < 0$, meaning that $k_{m'_r}$ is imaginary creating an evanescent wave in region "1" and the mode is confined in region "0". The lowest order eigenmode confined by mesa region "0" takes its field profile as the form of a Bessel function

of first kind in the mesa regions and the factor of 4.810 comes from this lowest order Bessel function approximation. Using this approach, the gratings can be designed such that the mode is confined within the mesas and becomes evanescent outside the mesa.

However, this is only part of the story of mode confinement based on the cavities of Fig. 2.1 (b) or (c), and Eq. 2.5 considers only the dominant coupling of the mode from region "0" to region "1". Not all of the wave from region "0" couples into the field of region "1" with the vertical wavevector component $k_{m'_z}$ because of non-orthogonality in the optical modes between the two regions. A small fraction of the field from "0" couples into other longitudinal modes of "1", and these other modes cause scattering loss. This scattering is why the effective index fails as an accurate design model for high performance VCSELs. However, it was shown recently [1] that this scattering loss can be minimized or made lower compared to oxide confined VCSELs by using very thin phase shifting layers. In the grating VCSEL to be discussed in chapter 3, a 65 Å thin layer has been used to obtain mode confinement by creating a resonant shift of 10 nm. Even thinner layers may be used to reduce the scattering loss. This has the additional benefit of improving crystal quality on top of the mesas.

2.2 Theoretical modeling of transverse modes

Modeling of a 1-D grating placed in a VCSEL cavity has been done to analyze its transverse modes. A schematic of the top view of the gratings is shown in figure 2.1 (a), while it's cross sectional view as shown in figure 2.2 (b). If $L_{1,1}$ is the length of the first mesa region and $L_{2,1}$ is the length of the first gap region, a transfer matrix of the electric and magnetic fields can be written based on Maxwell's equations in each of the regions. It is assumed that the grating is in the x-direction and a plane wave exists in the y-direction with the z-direction coming out of the page. The VCSEL cavity is taken in the z-direction for boundary condition analysis. The vertical cavity sets the vertical wave vector components of the field in both the mesa and off-mesa regions because of the high reflectivity mirrors. The transverse wave vector components in the x-direction are real, k_x, in regions "1" inside the mesas and imaginary, $i\alpha_x$, in off-mesa regions "2". These wave vector components are related by

$$\frac{\omega^2 n^2}{c^2} = k_x^2 + k_{1,z}^2 = -\alpha_x^2 + k_{2,z}^2 \tag{2.6}$$

where n is the average refractive index of the cavity. Considering a transverse electric field in the y-direction, the eigenmodes of the structure can be found by solving Maxwell's equations in the transfer matrix formulation.

Maxwell's equations can be written as

$$\nabla \times \mathrm{E} = i\omega\mu_o \mathrm{H} \tag{2.7}$$

$$\nabla \times \mathrm{H} = -i\omega\varepsilon \mathrm{E} \tag{2.8}$$

where E, H are the electric and magnetic fields respectively.

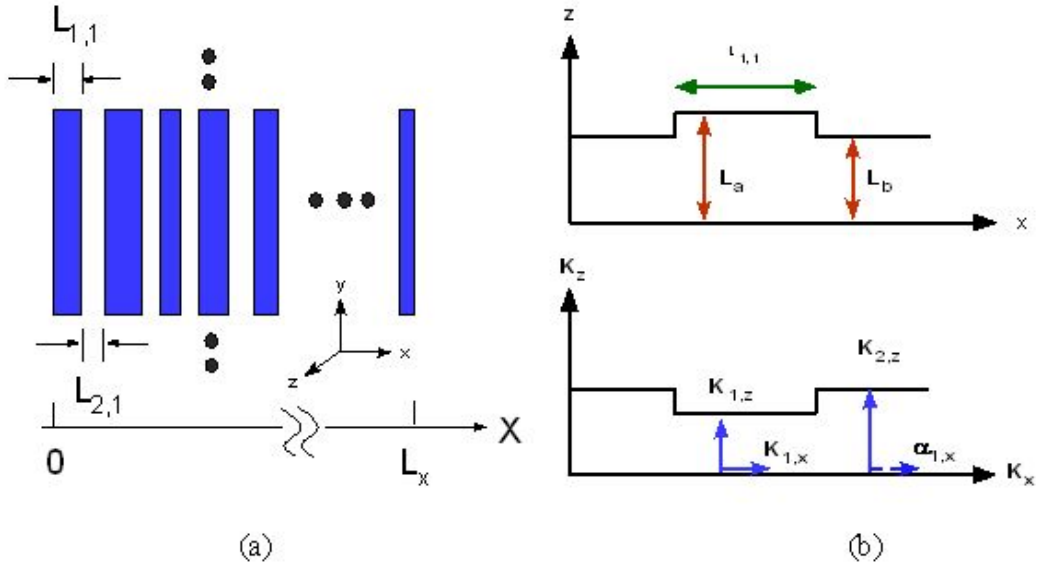

Figure 2.2: Schematic of (a) top view (b) cross-sectional view of a 1-D grating

Electric and magnetic fields can be expressed as forward and backward propagating waves.

$$\mathrm{E} = \mathrm{E}^{+} \exp(ik_x x) + \mathrm{E}^{-} \exp(-ik_x x) \tag{2.9}$$

$$\mathrm{H} = \mathrm{H}^{+} \exp(ik_x x) + \mathrm{H}^{-} \exp(-ik_x x) \tag{2.10}$$

$$ik_x \mathrm{E}^+ = i\omega\mu_o \mathrm{H}^+ \tag{2.11}$$

$$-ik_x \mathrm{E}^- = i\omega\mu_o \mathrm{H}^- \tag{2.12}$$

$$\mathrm{E}(x) = \mathrm{E}^+(x) + \mathrm{E}^-(x) \tag{2.13}$$

$$\mathrm{E}(x) = \mathrm{E}^+(x_o)\exp(ik_x(x-x_o)) + \mathrm{E}^-(x_o)\exp(-ik_x(x-x_o)) \tag{2.14}$$

$$\mathrm{E}(x) = [\mathrm{E}^+(x_o) + \mathrm{E}^-(x_o)]\cos(k_x(x-x_o)) + i[\mathrm{E}^+(x_o) - \mathrm{E}^-(x_o)]\sin(k_x(x-x_o)) \tag{2.15}$$

$$\mathrm{E}(x) = \mathrm{E}(x_o)\cos(k_x(x-x_o)) + i\frac{\omega\mu_o}{k_x}\mathrm{H}(x_o)\sin(k_x(x-x_o)) \tag{2.16}$$

$$\begin{bmatrix} \mathrm{E}(x) \\ \mathrm{H}(x) \end{bmatrix} = \begin{bmatrix} \cos(k_x(x-x_o) & i\frac{\omega\mu_o}{k_x}\sin(k_x(x-x_o) \\ -i\frac{\omega\mu_o}{k_x}\sin(k_x(x-x_o) & \cos(k_x(x-x_o) \end{bmatrix} \begin{bmatrix} \mathrm{E}(x_o) \\ \mathrm{H}(x_o) \end{bmatrix} \tag{2.17}$$

Using the above expression, we can relate the fields within the grating layers as

$$\begin{bmatrix} E_y(L_x) \\ H_z(L_x) \end{bmatrix} = \begin{bmatrix} \cos(k_x L_{1,1}) & \mathrm{i}\frac{\omega\mu_o}{k_x}\sin(k_x L_{1,1}) \\ \mathrm{i}\frac{k_x}{\omega\mu_o}\sin(k_x L_{1,1}) & \cos(k_x L_{1,1}) \end{bmatrix} \begin{bmatrix} \cosh(\alpha_x L_{2,1}) & -\frac{\omega\mu_o}{\alpha_x}\sinh(\alpha_x L_{2,1}) \\ \frac{\alpha_x}{\omega\mu_o}\sinh(k_x L_{2,1}) & \cosh(\alpha_x L_{2,1}) \end{bmatrix} \cdots \begin{bmatrix} E_y(0) \\ H_z(0) \end{bmatrix}$$

where $H_z(0) = \mathrm{i}\frac{\alpha_x}{\omega\mu_o} E_y(0)$ and $H_z(L) = -\mathrm{i}\frac{\alpha_x}{\omega\mu_o} E_y(L)$.

(a)

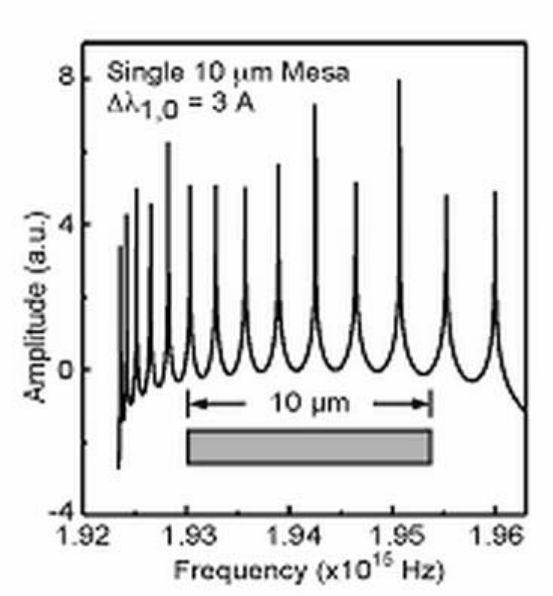
Single 10 μm Mesa
Δλ1,0 = 3 A
8
4
0
-4
Amplitude (a.u.)
10 μm
1.92
1.93
1.94
1.95
1.96
Frequency (x10^15 Hz)

(b)

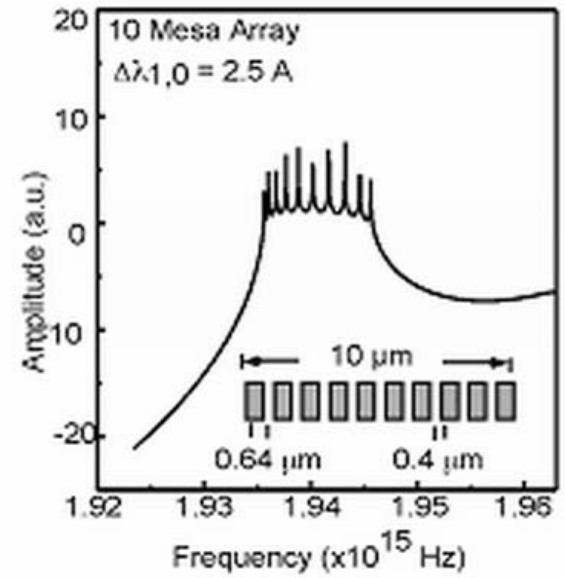
10 Mesa Array
Δλ1,0 = 2.5 A
20
10
0
-10
-20
Amplitude (a.u.)
10 μm
0.64 μm
0.4 μm
1.92
1.93
1.94
1.95
1.96
Frequency (x10^15 Hz)

(c)

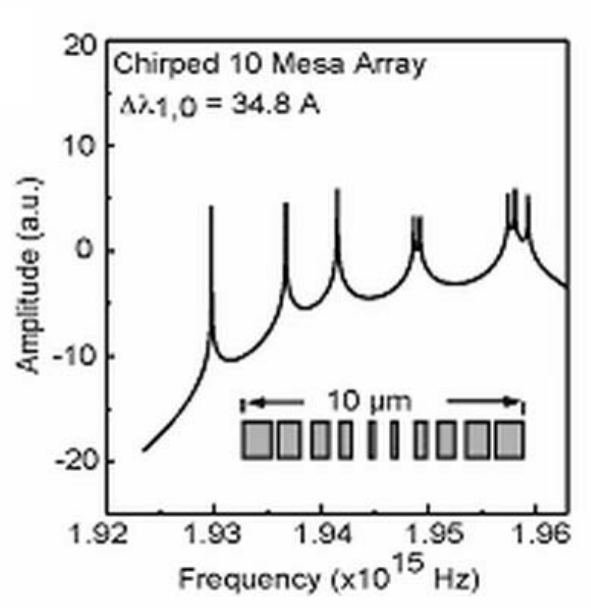

Figure 2.3: Plots of eigenmodes vs. frequency for different 1-D gratings. (a) a single 10 μm mesa (b) a uniform 10 μm mesa array (c) a chirped 10 μm mesa array.

This matrix formulation allows to determine the eigenmodes of a 1-D PC or grating formed from the intra-cavity mesas. Figure 2.3 shows plots for three different cases, comparing a 10 μm long single mesa in (a) with a 10 μm long, uniformly spaced 1-D grating in (b) and a chirped 1-D grating in (c). These calculations represent the mode structures of actual 1-D mesa designs for a 0.98 μm VCSEL. The optical modes are the spectral positions where the amplitudes go to infinity due to resonance. While the 10 μm long mesa of figure 2.3 (a) is multimode with a nearly uniform mode distribution, the uniform 1-D PC of figure 2.3 (b) shows mode grouping around a narrow range of frequencies. The chirped grating in figure 2.3

(c) shows the possibility of achieving single mode operation even with a 10 μm long active region. A 34.8 Å separation is obtained between the lowest order and next higher order transverse modes. As expected, the internal grating or PC can be designed to gain control of the transverse mode pattern. These 1-D lateral PCs and gratings can also readily be implemented into the VCSEL cavity and these can exhibit interesting modal behaviors. This calculation can be extended to two dimensional gratings or any other pattern. It is possible to obtain high single mode output by using a larger active area confined by a grating. A different design may be used to obtain multi-mode emission even with smaller device dimensions for high speed operation. Optical gain can also be included in the transverse matrix to predict the lasing spectra of the actual lasers.

CHAPTER 3

EPITAXIAL REGROWTH PROCESS AND DEVICE FABRICATION

3.1 Crystal Growth and Device Fabrication

This section gives an overview of the fabrication process of GaAs based laser diodes which incorporate epitaxial regrowth over shallow mesas. The steps that have been developed to implement the process are versatile and can be extended to fabricate different kinds of novel lasers. For all the devices, fabrication starts with crystal growth of the first part of the laser structure. This is followed by lithography and etching to create the intra-cavity gratings. The third step is the second stage of epitaxial growth to complete the laser structure. Once the growth is complete, rest of the fabrication involves metallization of contacts and isolation of devices. All the devices discussed in this dissertation were grown by molecular beam epitaxy (MBE) crystal growth technique on GaAs substrates using the Veeco GEN III system. The first stage of crystal growth includes either bottom DBR AlAs/GaAs mirror pairs or AlGaAs cladding layers, cavity with active region, mesa forming layers followed by sacrificial layers of $Al_{0.7}Ga_{0.3}As$ and GaAs. These sacrificial layers which are also etch-stop layers are used to obtain a clean interface for regrowth. All the layers in the first stage of growth are grown at normal growth temperature of 590 ^{o}C which is ten degrees higher than the GaAs desorption

temperature except for InGaAs/GaAs quantum well active region that is grown at 520 ^{o}C to prevent indium evaporation.

After the first growth is complete, e-beam lithography was used to create the intra-cavity grating patterns. The exposures were done using JEOL 6000 FSE-E-beam lithography system. To create mesas, negative e-beam resist NEB 31A is spun at 3000 rpm for 30 sec to obtain a thickness of 2000 Å. The resist is prebaked at 110 ^{o}C for 2 min and the pattern is written with an e-beam current of 75 pA at 50 kV. The sample is then developed using MIF 300 solution for 40 sec and rinsed with DI water. Alternately, openings can also be made in the top layers and a positive photoresist was used for this purpose. Positive tone e-beam resist ZEP 520A was spin coated at 3200 rpm for 30 sec to obtain a thickness of 3000 Å. The resist was prebaked at 180 deg C for 2 min. The patterns were exposed using a 50 kV e-beam at 100 pA. It is then developed in ZED-N50 for 2 min, and rinsed with isopropyl alcohol for 30 sec.

The top GaAs layer is then etched using a 5:1 solution of citric acid solution (which is a 1:1 solution by weight of citric acid monohydrate and water) and hydrogen peroxide solution. This etchant has a 200 to1 selectivity ratio with respect to etching GaAs and $Al_{0.7}Ga_{0.3}As$ respectively [36]. The photoresist is stripped using acetone and the sample is placed in oxygen plasma for 5 min to remove any organic residue. The sample is then placed in a solution of 1:20 HF:H_2O to etch the underlying $Al_{0.7}Ga_{0.3}As$ layer. This solution etches only high Al composition

AlGaAs and does not etch GaAs. So, the top GaAs layer acts as a mask for etching the grating mesas into the top two sacrificial layers. This is followed by another etching sequence of GaAs and AlGaAs layers. In this fashion, the sacrificial layers act as etch masks to transfer the photonic pattern to the actual mesa layer. A schematic representation of this selective etching process is shown in figure 3.1. Another variation for the process just described is used with low composition AlGaAs layers (Al: 30-40%) for obtaining current confinement. This is discussed further in section 3.2 for the fabrication of grating confined VCSEL. The selective etchant for this material is a solution of 3:1 citric acid: H_2O_2, and this has good selectivity to high Al-composition AlGaAs.

By using selective etching process, the mesa layer that has the grating patterns does not come into direct contact with photoresist and other processing; so contamination of the mesas is minimized. This is important to have a good quality crystal for regrowth. The selective etch process also has the advantage that it gives a good control over layer thicknesses. Since wet etching is used there is always some undercut, but that was taken into account while determining the feature sizes for the patterns. This will not be an issue if reactive ion etching is used, the only requirement would be to have the same selectivity that is possible with the wet etching. After the final etch step, we have a pristine surface that is ready to be placed back in the MBE chamber for regrowth.

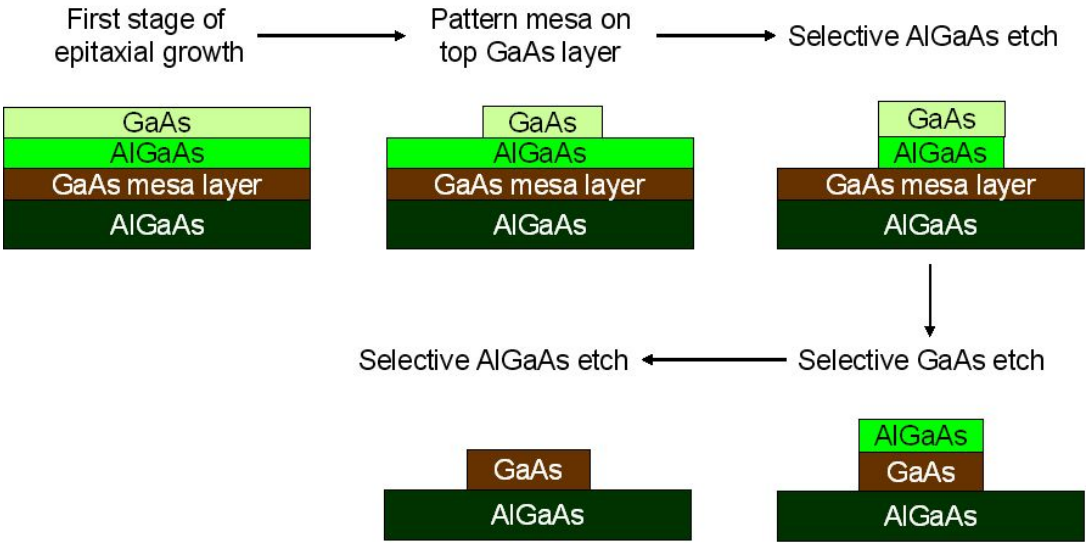

Figure 3.1: Schematic of selective etching process for regrowth

3.2 Optimization of Epitaxial regrowth Process

It is very important to have a high crystal quality after the processing to be able to grow defect -free single crystal material on top of the mesas. Any scattering due to interface roughness increases internal loss in the device and degrades device performance. Epitaxial regrowth on non-planar substrates is complex compared to that on planar substrates. Crystal growth on patterned surfaces depends on various factors. During the course of this study, it was found that this depends on the type of atoms that are being incorporated, the underlying layer, and also on the feature sizes of patterns. While studying quantum dot microcavities of different dimensions,

it was observed that the nature of overgrowth depends on cavity sizes. This is covered in more detail in section 4.2.

In MBE growth, constituent elements of a semiconductor in the form of molecular beams are obtained by thermal evaporation of elemental sources [37]. These are deposited in an ultra-high vacuum environment onto a heated crystalline substrate to form thin epitaxial layers. The growth process involves four steps [38]; absorption of impinging molecules on the heated substrate, surface migration of the impinging molecules and dissociation of the absorbed molecules, incorporation of molecules into stoichiometric crystal lattice site, and desorption of excess molecules from the crystal surface.

For growth of GaAs based materials, migration of group III elements is the rate limiting step since group V atoms are very volatile. Mobility of group III atoms depends on the crystallographic orientation of the planes on which they are being incorporated. Group III atoms tend to migrate from less reactive facets to more reactive neighboring ones. This gives rise to different sticking coefficients on different planes, and could lead to preferential growth on certain planes. So, it is very important to control the kinetics of the growth process to maintain the surface morphology. Another factor that affects growth is the nature of the surface on which the atoms are being deposited. It was experimentally observed that Ga atoms have a strong tendency to bond to GaAs compared to AlGaAs surface. This could lead to over-growth at an AlGaAs-GaAs interface and this gives rise to scattering

losses due to discontinuity of E-field at the boundaries. Using a lower temperature growth or a higher arsenic flux can reduce the mobility of ad-atoms due to a decrease of the migration length of adatoms, and prevent preferential growth. In a previous attempt, regrowth was performed at 600 ^{o}C [39], and roughness along the aperture edge resulted along one crystal direction mainly due to the difference in the migration length and sticking coefficient of adatoms on different crystal planes [40]-[42]. In order to obtain a smooth profile and good crystal quality over the grating mesas, regrowth is performed at 470 ^{o}C, lower than the normal growth temperature. The difference in regrowth quality at various temperatures can be easily observed using an optical microscope and it was found that a reduced regrowth temperature is important for eliminating crystal discontinuity at the mesa perimeters.

3.3 Intra-cavity Grating Confined VCSEL

Figure 3.2 (a) shows a schematic illustration of the grating-confined all-epitaxial VCSEL, while (b) shows a scanning electron microscope image of the epitaxial intracavity grating prior to regrowth [43]. Crystal growth is performed on an n^{+} GaAs substrate. The epitaxial layers that make up the device from the initial growth consist of a lower 26.5 pair n-type AlAs/GaAs quarter wave mirror stack, an $Al_{0.05}Ga_{0.95}As$ one–wavelength cavity spacer with three InGaAs/GaAs quantum wells emitting at 980 nm placed at its center, an upper p-type $Al_{0.7}Ga_{0.3}As$

confining layer, an upper p-type $Al_{0.3}Ga_{0.7}As$ layer, and a 65 Å thick p-type GaAs phase shifting mesa layer. The n- layers were doped with silicon, and the p-layers were doped with carbon using a carbon tetrabromide source. After the initial growth, e-beam lithography is used to form circular gratings in the p-type GaAs phase shifting mesa layer. The wafer is then returned to the MBE system for regrowth, with the surface consisting of the p-type GaAs phase shifting mesa layers and outside these mesa regions the p-type $Al_{0.3}Ga_{0.7}As$ layer. An epitaxial regrowth then completes the upper mirror by depositing an additional 16.5 pairs of p-type AlAs/GaAs mirror pairs. The fabrication procedure is completed by depositing AuGe/Ni/Au n-contact on the back side of the wafer which is annealed at 400 ^{o}C for 30 sec and a 60 μm/30 μm ring p-contact of Ti/Au on the top surface that is concentric with the grating. Metal deposition was done using e-beam evaporation. Individual devices are then isolated by etching down through the active region by an isotropic etch solution of 1:8:80 H_2SO_4: H_2O_2: H_2O. The grating confined VCSEL has a 15 μm diameter with the inner mesa being 4 μm and three 1.25 μm outer rings that are spaced 0.6 μm apart. On the same wafer and adjacent to the grating confined VCSELs, 10 um single mesa VCSELs are also fabricated for comparison.

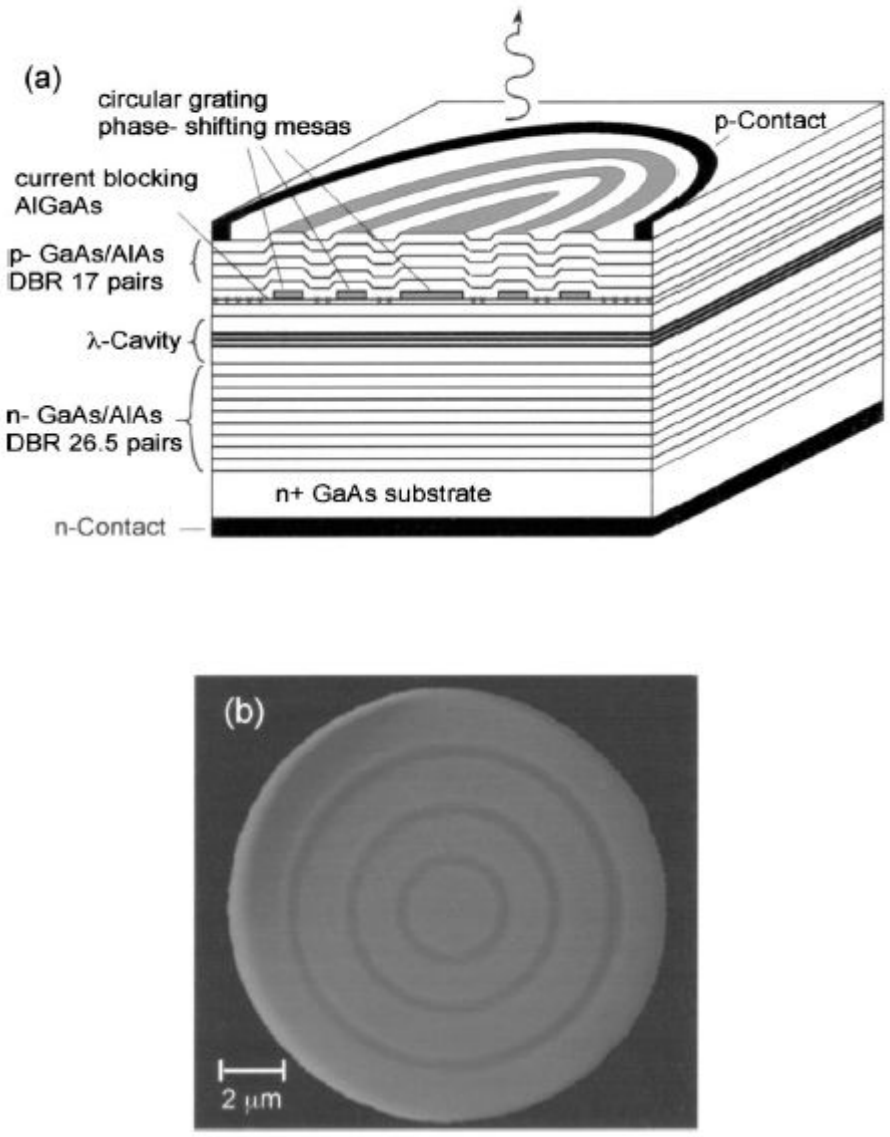

Figure 3.2: (a) Schematic of an all-epitaxial VCSEL with a circular grating phase-shifting mesa. (b) Scanning electron micrograph image of a circular grating fabricated by electron-beam lithography.

3.3.1 Current confinement within gratings

Electrical confinement is obtained to the intracavity GaAs phase-shifting mesas through selective Fermi-level pinning at the $Al_{0.7}Ga_{0.3}As$/GaAs regrown heterointerface. After patterning the grating mesas, there is always native oxide on the surface before it is removed in the MBE chamber by thermal desorption for the second step of crystal growth. This process is normally done at 580 ^{o}C in As overpressure to remove the native oxide. The native oxide is removed easily on GaAs, however, it is not completely removed on AlGaAs surface because aluminum forms a strong bond with oxygen which is hard to remove by thermal desorption. Therefore when GaAs is grown on top of it, there are many missing bonds, and this forms interface states in the band gap. So Fermi level of this interface is pinned in the mid gap regardless of doping. A schematic of the regrowth surfaces can be seen in figure 3.3 while the equilibrium band diagram in the off-mesa regions is shown in figure 3.4. This interface Fermi-level pinning depletes the crystal region around the interface, and combined with the large valence band offset between $Al_{0.3}Ga_{0.7}As$ and GaAs leads to a large forward voltage for easy current flow. The turn on voltage is determined by doping level and thickness in p -AlGaAs layer and the Al composition. Al composition around 20% - 40% was found to be an optimum value by taking into consideration the crystal quality as well.

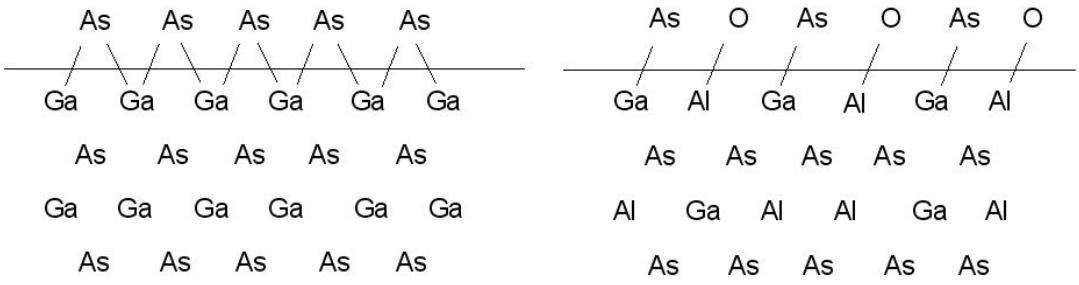

Figure 3.3: Schematic of regrowth interfaces (a) GaAs in the mesa region and (b) $Al_{0.3}Ga_{0.7}As$ in the off-mesa regions

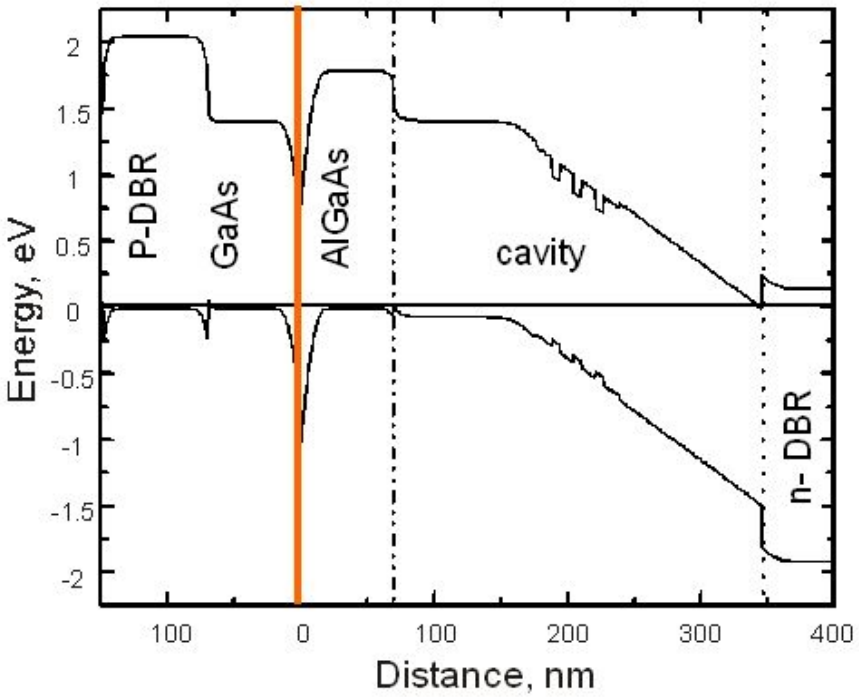

Figure 3.4: Schematic of equilibrium energy band diagram outside the mesa regions where Fermi-level is pinned.

Test structures show that the forward voltage for easy current flow in the region of the $Al_{0.7}Ga_{0.3}As$/GaAs regrown interface exceeds 4.5 V, while for the GaAs phase-shifting mesa it is ~1.2 V. The individual VCSELs are isolated using 100 μm pillars etched through the active region, and no other current confinement is used. Figure 3.5 shows the current-voltage characteristic measured either in the actual device (on the mesa grating) or through a current-blocking test region electrically isolated from the mesa grating. The test structure consists of a 60 μm diameter etched post with a 30 μm diameter metal contact, and passes little current for bias voltages less than 5 V. The test structure therefore includes an area outside the mesa that is 16 times larger than the 15 μm grating confined VCSEL, and demonstrates that the current injection is effectively confined to the mesas to enable tailoring of the injected current with this intracavity grating technique. It is to be noted that a deep proton implant can be used to isolate the devices and produce a fully planar wafer that would be attractive to minimize parasitic capacitance.

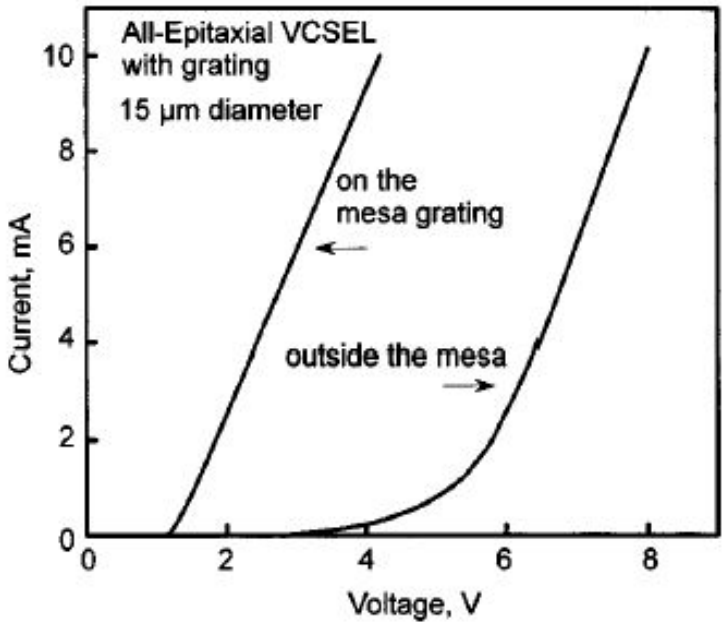

Figure 3.5: Current vs. voltage characteristics measured for the 15 μm mesa grating VCSEL (on the mesa grating) and a 60 μm diameter etched post formed outside and electrically isolated from the mesa grating.

3.3.2 Device Characterization

Numerous devices are tested and good uniformity is found both for the 15 μm grating confined and 10 μm simple mesa confined VCSELs. Figure 3.6 shows the continuous wave light versus current curves for both devices. The threshold current of the 15 μm diameter grating confined VCSEL is 1.74 mA, which corresponds to a threshold current density of 985 A/cm^2, while the 10 μm diameter simple mesa confined VCSEL has a threshold current of 0.7 mA that corresponds to 891 A/cm^2. The threshold voltage of the 15 μm diameter grating-confined

VCSEL of figure 3.2 is 1.4 V with a differential resistance of 148 V, although there is some variability in electrical resistance across the wafer. The threshold voltage of the 10 μm diameter simple mesa VCSEL is 1.6 V with a differential resistance of 450 V. The higher output power and threshold current of the 15 μm diameter grating confined VCSEL versus the 10 μm diameter simple mesa confined VCSEL simply track approximately the factor of 2.2 increase in active area. On the other hand, the increase in slope efficiency for the grating confined VCSEL, which is

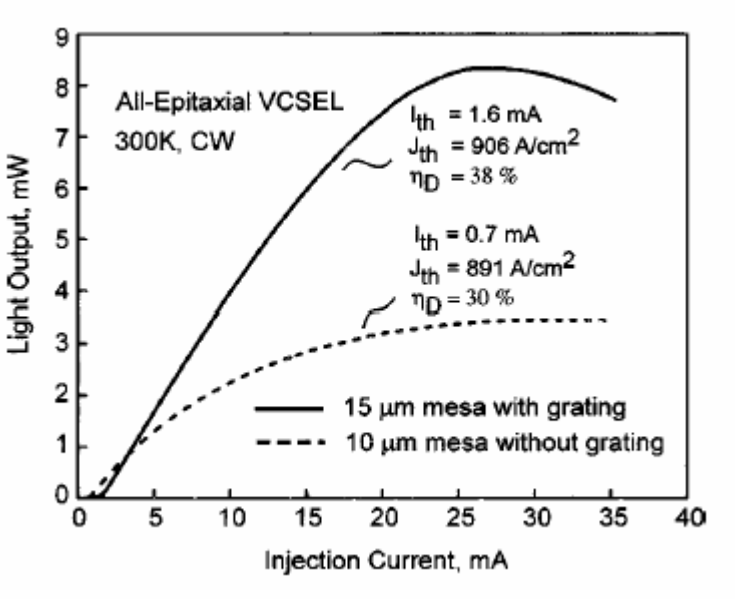

Figure 3.6: Light vs. current characteristics measured for all-epitaxial VCSELs with a 15 mm grating (solid curve) and 10 mm single mesa (dashed curve).

consistently found for side-by-side devices, does not. This increase in slope efficiency appears to come from the smaller feature sizes of the grating confined VCSEL that lead to an improved mode control and more efficient pumping of the grating confined VCSEL's lasing modes.

Figure 3.7 shows the spectral output of the grating-confined VCSEL, while figure 3.8 shows far-field radiation patterns at the same drive currents for either VCSEL. Both the grating-confined and simple mesa VCSELs are multimode with similar lasing spectra, while the far-fields are indicative of the coherent spot sizes of the multiple transverse modes. The narrower far-field pattern of the grating confined VCSEL indicates larger near-field coherent spot sizes. For a Gaussian fundamental mode, the size of the near field mode is given by $D = \frac{4\lambda}{\pi\theta}$, where D is the diameter of the near field modal intensity measured at the $1/e^2$ angular width, λ is the wavelength of the emitted light, and Θ is the angular width of the far field intensity in radians measured at $1/e^2$. The far-field of the 10 μm simple mesa corresponds to a spot size of ~3 μm, while that of the 15 μm grating confined VCSEL corresponds to ~8 μm. We note that the 4 μm diameter of the inner area of the grating confined VCSEL (figure 3.2 (b)) is close to the value of the 3 μm coherent spot size of the simple mesa, while the 1.5 μm rings are less than this value. This shows that optical coupling exists between the rings in the grating confined VCSEL. The increase in efficiency of the grating confined VCSEL is

therefore consistent with reduced spatial hole burning and greater mode overlap in the grating confined device, despite its larger area and multimode operation. This is perhaps not too surprising, given that introducing the grating provides additional boundary conditions for the transverse modes and current injection.

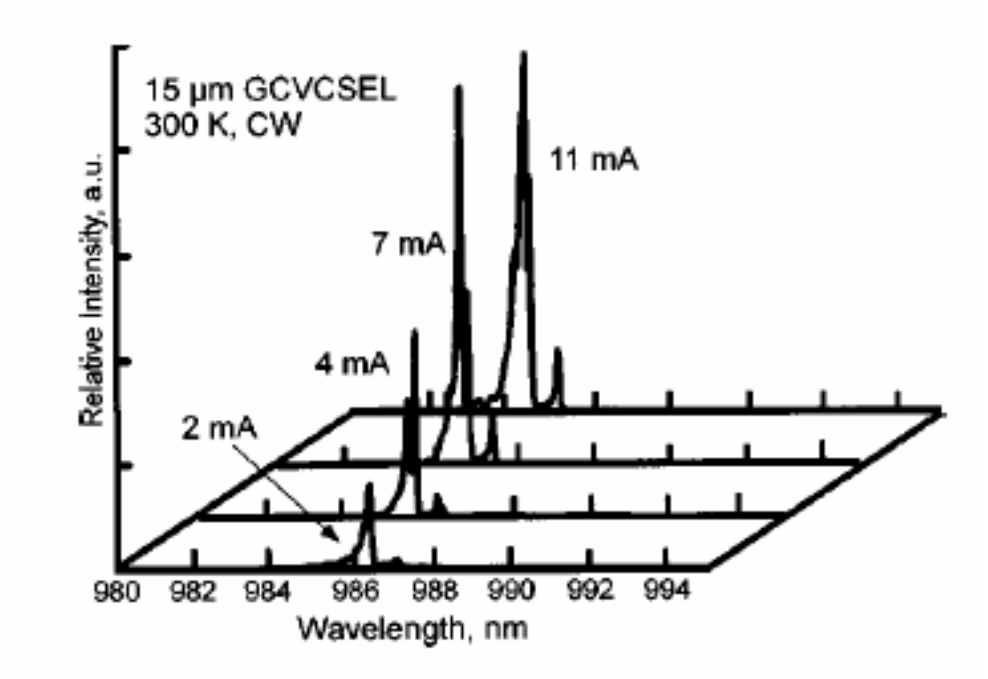

Figure 3.7: Spectral data measured for the 15 µm grating confined VCSEL at the current levels of 2, 4, 7, and 11 mA.

We also note that despite the higher efficiency of the grating confined VCSEL, we measure a consistent slight increase in its threshold current density. Recently, we compared the theoretical scattering loss in this type of an all-epitaxial, mesa confined VCSEL with that of oxide-confinement [31]. The analysis shows why in the ideal case the all-epitaxial approach will exhibit lower optical loss. To further characterize the optical loss due to the regrowth, which may be mostly due to optical scattering from a roughened interface, we have also performed additional experiments on edge-emitting lasers using a similar regrowth. The edge-emitters allow us to accurately extract the optical loss, at least for those devices. Those experiments show that a similar, though not identical, regrowth increases the internal waveguide loss of the edge-emitters from ~3 cm^{-1} to ~8 cm^{-1}. The likely source of additional waveguide loss is a slightly increased optical scattering loss, to which the VCSEL would be extremely sensitive. This is consistent with the present results of slightly higher threshold current density on the grating confined VCSEL if the optical scattering is further increased by the inclusion of the grating. Therefore, the present results may be substantially improved once the epitaxial regrowth is optimized for ideally smooth interfaces. Finally, we point out that we have not made an attempt to optimize the grating design for high efficiency or low threshold, and in fact the present design does neither. Instead it is used to demonstrate the potential of a new fabrication approach to open the design space in

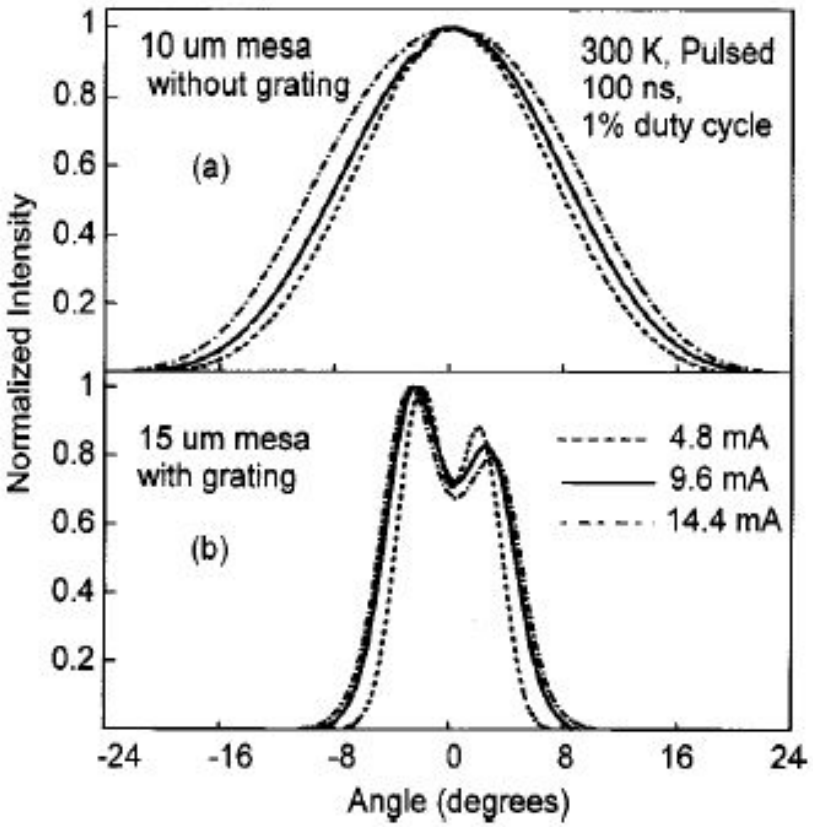

Figure 3.8: Far-field radiation patterns measured at different current levels. Similar patterns are measured for the orthogonal direction. (a) shows the profile for a 10 μm simple mesa, while (b) is for the device with a 15 μm grating.

engineering high performance VCSELs through simultaneous control of their mode and gain profiles. The present design still has the same radius-squared problems discussed in chapter 1, and even finer chirped gratings must be developed to optimize the VCSEL performance. For example, in the present 15 μm diameter grating confined VCSEL that includes the 4 μm diameter center region and three 1.25 μm diameter outer rings with 0.6 μm spacings, a uniform threshold current density for the 1.74 mA current leads to 124 μA injected into the 4 μm center region, 296 μA in the third ring, 393 μA in the next ring, and 536 μA in the outer most ring. The resulting gain profile, with most of the current and therefore the optical gain in the outer most ring, clearly is unfavorable for a lowest order optical mode confined in the grating. This can be avoided by use of a chirped grating with decreasing outer ring sizes. This type of VCSEL can lead to improvements in the transverse overlap between the optical mode and gain to provide increased single mode selectivity, lower threshold, and improve the device efficiency.

3.4 Laser diode with buried etched void photonic crystal pattern

The epitaxial regrowth process with intra cavity gratings or photonic crystals can also be extended to broad area distributed feedback (DFB) lasers, even without a vertical cavity. DFB lasers typically generate output with increased stability and at more precisely controlled wavelengths than regular diode lasers. The lasers incorporate a grating in the design such that feedback from the grating causes

interference that promotes gain at a wavelength related to the period of the grating. Usually, however, the grating (and the feedback) occurs in only one dimension. Two dimensional photonic pattern controls not only the longitudinal mode, like in linear DFB lasers, but also the lateral mode. So they can be used to make multidirectional DFB lasers, which could provide high-power surface-emitting lasers with narrow wavelength bandwidths [44]. Broad area surface emitting lasers are important for high power output, low beam divergence and also for short-distance high-speed links using multimode fibers. However, the photonic crystal based devices made so far have been either optically pumped [45,46] or involved wafer fusion for current injection [44],[47],[48]. The all-epitaxial regrowth approach provides an elegant alternative for electrical injection with fairly simple processing. The photonic pattern can be placed close to the active region, where the electric field is strongest, and enhance its interaction with the optical mode.

The epitaxial growth is performed on an n+ GaAs substrate. The first stage of growth consists of a 2 μm cladding layer of n-type $Al_{0.35}Ga_{0.65}As$, followed by a wavelength cavity spacer of GaAs with three 80 Å $In_{0.2}Ga_{0.8}As$/ 100 A GaAs quantum placed at its centre, and an upper p-type confining layer of $Al_{0.35}Ga_{0.65}As$ of thickness 740 Å, a thin p-type layer of GaAs of thickness 100 Å, and an $Al_{0.7}Ga_{0.3}As$ layer of thickness 500 Å. A p-type GaAs layer of thickness 100 Å completes the first growth. All the layers were grown at 590 ^{o}C. After this initial growth, circular openings are defined on the top GaAs layer using electron-beam

lithography. The patterns consist of areas of 50 μm x 2 mm regions of 100 nm diameter holes on a square lattice with a lattice constant of 300 nm. Following patterning of the resist, the upper GaAs and $Al_{0.7}Ga_{0.3}As$ layers in the patterned regions are removed by selective wet etch process. The sample is then placed back in the MBE system for epitaxial regrowth of p-type GaAs and $Al_{0.35}Ga_{0.65}As$ cladding layers to complete the laser structure. After thermal desorption of the native oxide at 580 ^{o}C, the substrate temperature is reduced to 470 ^{o}C to grow the first 400 Å of GaAs. This reduces the mobility of Ga ad-atoms to form a smooth surface morphology that preserves the growth front parallel to the photonic pattern. After this, the growth temperature was increased back to 590 ^{o}C. This is done to activate carbon atoms for p-doping and also to obtain a better crystal quality. The top layer that completes the growth is heavily doped p+ GaAs for forming electrical contact. The fabrication process begins with deposition of an n-contact Au-Ge 400 Å /Ni 100 Å /Au 1000 Å on the back side of the wafer. A 30 μm wide Cr 300 Å /Ag 2000 Å /Au 1000 Å stripe centered on the 50 μm wide grating region is then deposited on the top surface which serves as a p-contact by using lift-off technique. After this, photolithography is done to create 30 μm stripe openings along the length of each side of the 50 μm wide patterned regions. The sample is now etched using an isotropic wet etch consisting of 1:8:80 H_2SO_4:H_2O_2:H_2O. This etch exposes the underlying $Al_{0.7}Ga_{0.3}As$ layer for further processing. The sample is then placed in HF solution for selectively removing the $Al_{0.7}Ga_{0.3}As$ layer. This

selective etching of the $Al_{0.7}Ga_{0.3}As$ layer is a lateral etch that creates buried etched voids in the square lattice pattern, as shown in Fig. 3.9. These void regions are supported by GaAs posts formed by epitaxial regrowth, and this combination creates a mechanically stable etched void- semiconductor grating [51]. No special precautions, such as critical point drying, are needed to prevent collapse of the structure.

The finished laser diode is illustrated in figure 3.9. Ridge waveguide edge emitters of similar dimensions without any pattern are also fabricated from the same material in regions without the grating. These devices are used for direct comparison to determine the influence of the optical grating on the laser diode characteristics.

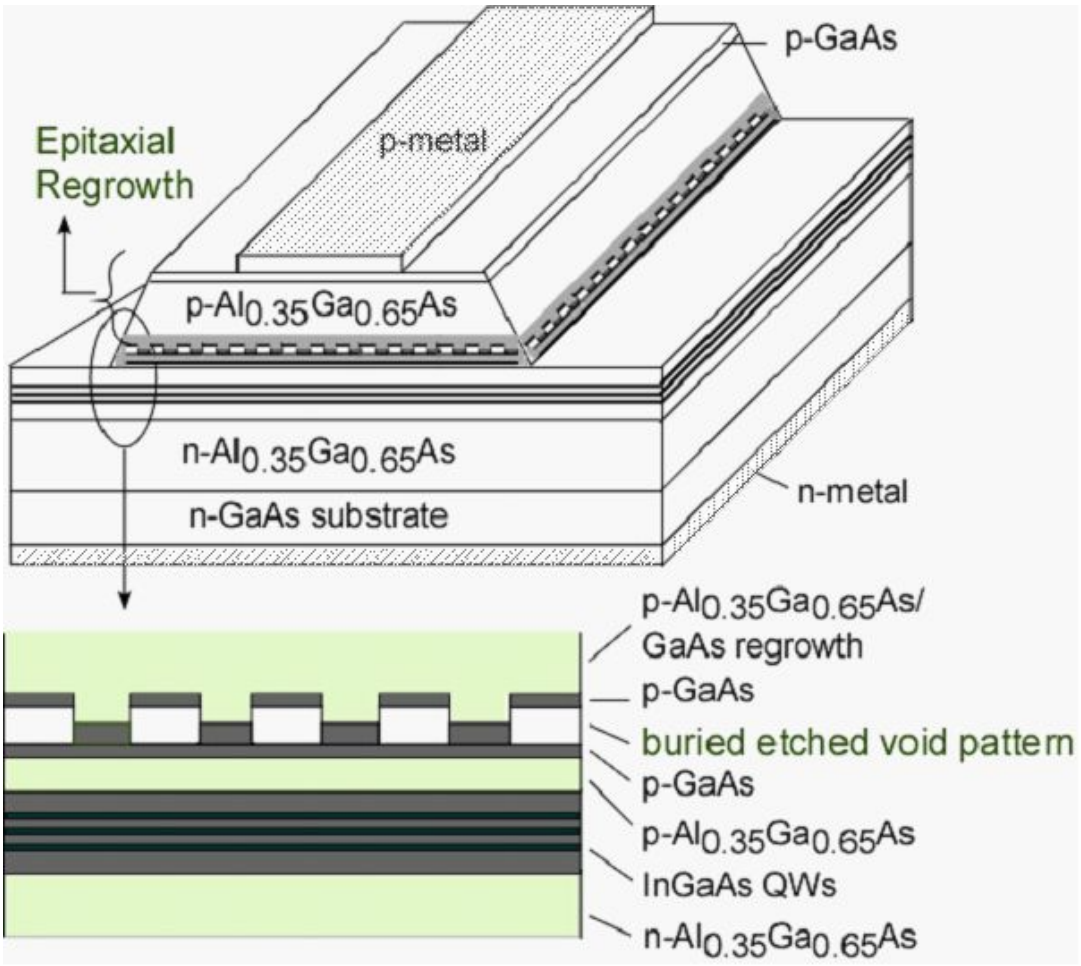

Figure 3.9: Schematic illustration of edge-emitting laser diode that includes buried etched-void photonic pattern

3.4.1 Effect of photonic pattern within the device

A 1-D or 2-D photonic crystal (PC) does not create a true energy gap, but modifies the E-k diagram of selected photon modes of interest. Although analogy is often made between a PC and an electronic crystal, there is a fundamental difference between Bosons and Fermions that occupy the modes. An electronic crystal mode can hold at most one electron, while a PC mode can be heavily populated by photons through stimulated emission. Therefore even a 1-D confined PC can channel nearly all of a system's energy into a single mode, while a 1-D confined electronic crystal (a superlattice with two degrees of freedom) cannot prevent electrons from occupying a large range of k-vector modes due to the in-plane motion perpendicular to it periodic structure. 2-D PCs have been studied by several groups, and the feedback from the lattice can support novel lasing [46]-[50].

The device structure was simulated using a plane wave expansion method [52,53] for the TE polarized modes. The computational domain consists of a unit cell with periodic boundary conditions. The cell has dimensions of a by a by 16*a, where a is the periodicity of the square lattice. The simulation assumes a supercell approximation, meaning that periodicity is enforced in all dimensions even though the structure isn't periodic in the vertical direction. This is not a problem as long as the mode is well-confined, and the supercell is sufficiently large so that there is negligible coupling between modes in adjacent cells. The calculated bands in the structure are shown in figure 3.10 (a). The calculation is performed over the

standard irreducible Brillouin zone of a square lattice. In the band diagram of figure 3.10 there are 18 calculated bands. They are spaced very tightly together, indicating that the structure has relatively low index contrast and supports many different modes. The points of low group velocity (in turn, maximized feedback) are the X and M K-points. The modes at the X point are mostly leaky (guided in the low index regions and the cladding) so it is of no interest. Several of the modes at the M point are well guided in the InGaAs QW [band 9 (shown as blue) to 16 (shown as green)]. These modes are shown in figure 3.10 (b),(c), where the electric field density is plotted at two cross-sections. Not all bands in this range are shown because several of them are degenerate. The top view is a plot of the mode sliced in the center of the InGaAs QW region (the outline of the holes is only shown as a reference). The side view is at the center of the rods. It is to be noted that there is a significant portion of the field in the substrate. This is believed to be an artifact of having a finite substrate size (1 μm) and would be reduced for even larger computational cells. Band 13 in figure 3.10 (b) is of interest because the amount of field concentrated around the InGaAs region is significantly higher than all of the others (all are plotted on the same scale). This may indicate that it is the point of maximized distributed feedback. Figure 3.10 (c) is a leaky mode where the field is concentrated in the low index air regions.

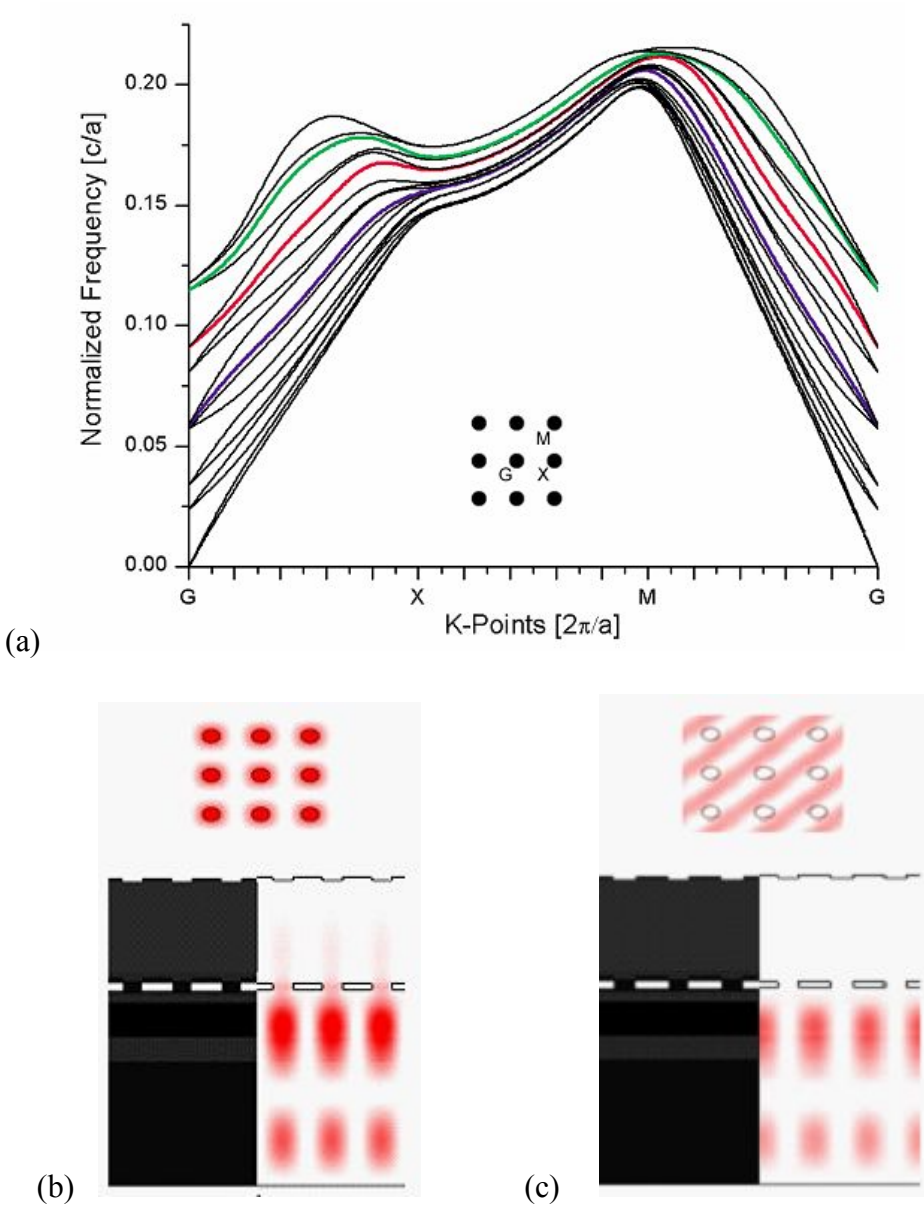

Figure 3.10: (a) Dispersion diagram for the laser structure with the photonic pattern (b) Electric field profile for a guided mode and (c) Electric field profile for a leaky mode.

Also, the mode in the InGaAs region of band 13 is centered on the rods. This band has a group velocity of 10^{-6} c. The other bands are on the order of 10^{-5} c, where *c* is the velocity of light in vacuum. When the quantum wells emit, all modes will be excited; the one with the highest interaction with the active region, i.e., the lower group velocity will lase. The frequency range for this criterion is dependent on the sizes of the photonic crystal and so the patterns can be designed to obtain desired modal characteristics.

3.4.2 Device Characterization

The light against current output characteristics for the devices are measured from the as-cleaved facets under pulsed conditions and are shown in figure 3.11. The threshold current density for a 1.6 mm-long device with the buried photonic pattern is 330 A/cm^2, and for a similar length device without any pattern it is 500 A/cm^2. Although the laser diodes fabricated from regions without the grating are quite uniform, we find that the variation in device performance for laser diodes with the grating is larger. The larger variation is likely due to process variation, which influences the actual grating dimensions. However, the experimental results demonstrate that there can be a significant reduction in threshold current for the laser diodes that incorporate additional cavity feedback due to the buried photonic pattern. We also find that the grating slightly improves the slope efficiency, which could be a result of the lower threshold and higher internal efficiency. The current–

voltage characteristics shown in figure 3.12 demonstrate that the electric resistance values of the etched pattern devices are similar to those of the unpatterned devices. This confirms that the etched void regions are firmly supported by the conductive GaAs posts and provide efficient current injection.

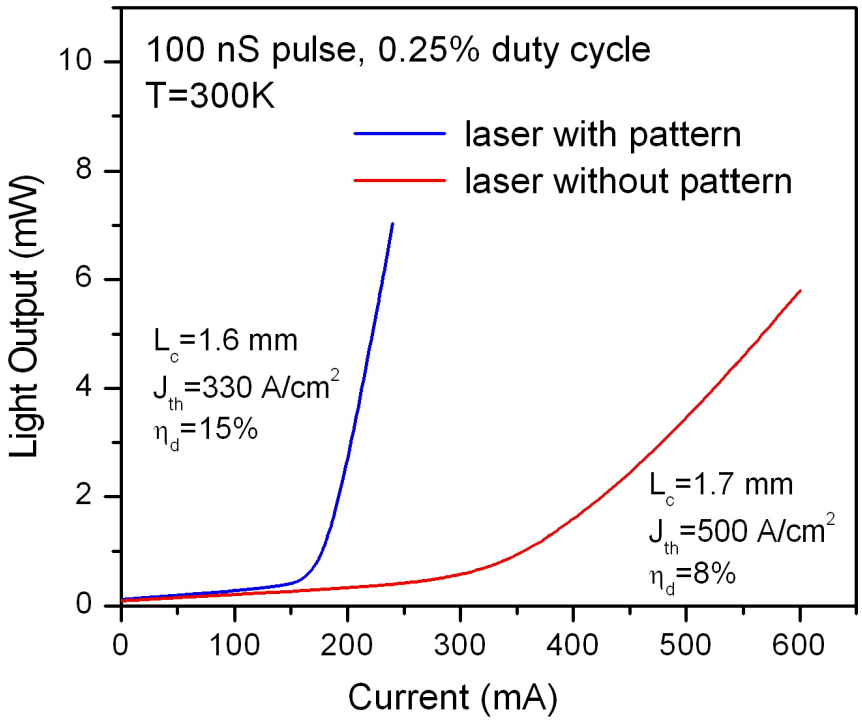

Figure 3.11: Light against current characteristics comparing laser diode that includes photonic pattern with another diode from same fabricated wafer but from a region without pattern.

The lasing spectrum of the device with the etched void pattern has fewer Fabry-Perot modes compared to the devices without the pattern as seen from figure 3.13, and shows that the etched-void photonic pattern indeed improves the modal selectivity through Bragg reflection. Although detailed design is required to improve coherence over a large area and to determine the area over which coherence can be obtained, these measurements show that the fabrication approach

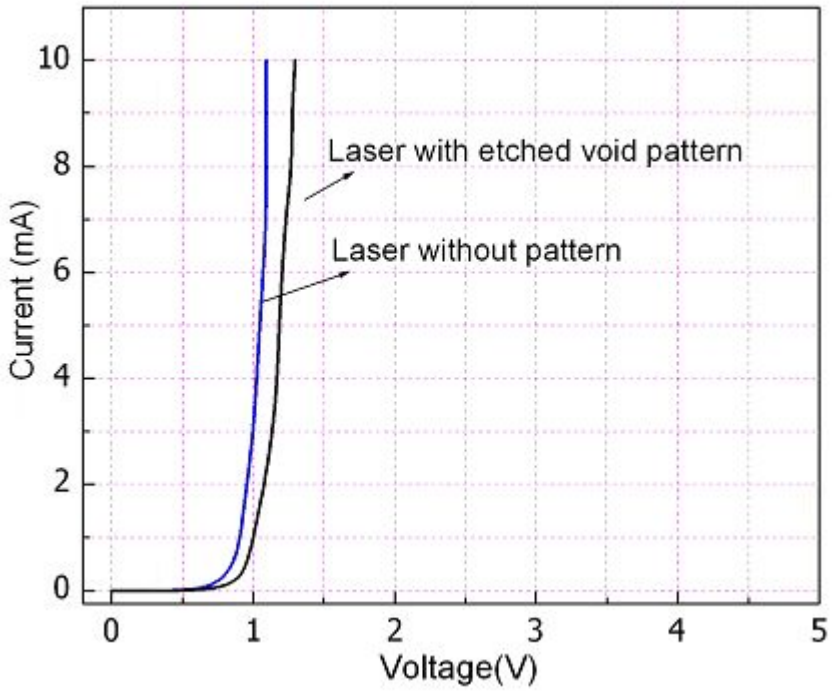

Figure 3.12: Current vs. voltage characteristics for laser diodes of figure 3.11.

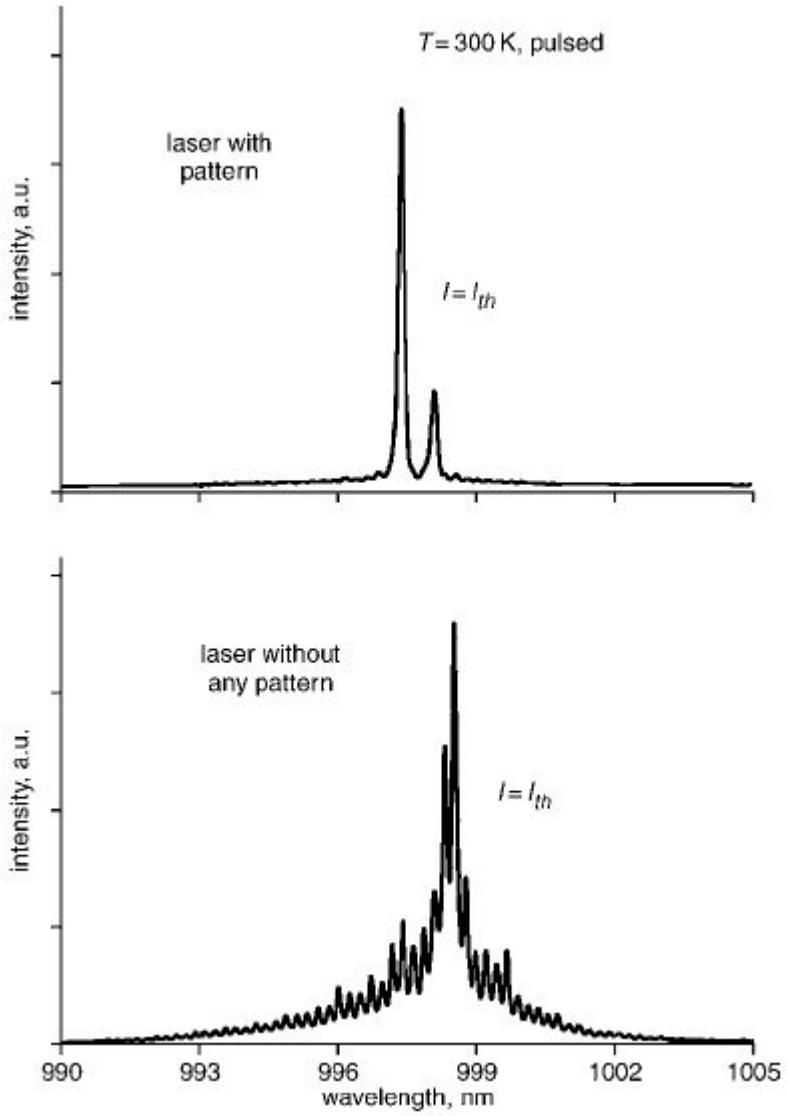

Figure 3.13: Spectral characteristics measured at threshold for laser diodes of figure 3.11.

could become important in introducing two-dimensional high contrast gratings in GaAs based devices. This technique also provides the means to obtain coherent surface light emission in a single mode by enabling uniform large area current injection. For certain designs of the photonic crystal, for example in a square lattice, light is also coupled out of the plane of the lattice normal to the substrate through upward diffraction since Bragg condition is also satisfied for this direction. This makes surface emission possible in these kinds of devices. This was examined by using upper DBR pairs in the device; however, surface emission was not obtained. This may be due to poor reflectivity of the top layers because of rough interfaces from high temperature regrowth. Use of low temperature through out the regrowth and not just the initial layers might create a smooth morphology for surface emission.

An important feature of the fabrication process is its mechanical robustness and ease of electrical injection, which creates the potential for transfer to a manufacturing environment. Similar fabrication techniques should also be possible in InP-based materials, which also offer high etch selectivity. This technique is also compatible with the fabrication of GaAs-based vertical-cavity surface-emitting lasers, by introducing upper and lower semiconductor mirrors. The only requirement is that the upper mirror be formed from the AlGaAs materials that satisfy the needed selectivity in etching.

CHAPTER 4

QUANTUM DOT BASED VCSELS WITH EPITAXIAL REGROWTH PROCESS

4.1 Introduction

Epitaxial InGaAs/GaAs quantum dots are attractive as single photon emitters due to their ease of fabrication and inclusion with monolithic microcavities, short spontaneous emission lifetimes, and the possibility of electrical injection. For example, it is possible to have fully isolated quantum dots that can be monolithically integrated with single electron transistors to create electronically controlled single photon sources. The efficiency of light output can be improved by placing the dots within a microcavity. This not only enhances the spontaneous emission properties through the Purcell effect but also allows photon emission into a single cavity mode. A key feature of these structures is the quality factor Q of the cavities which is given by the ratio between the mode wavelength λ and its linewidth $\Delta\lambda$. By using the epitaxial regrowth process, it is possible to create semiconductor microcavities by isolating one or more self-organized QDs in a shallow mesa, and covering this mesa with epitaxial mirrors to form a buried heterostructure VCSEL. This new type of QD microcavity has a high Q and the desirable features needed for commercial applications of being lithographically defined, all epitaxial and strain free, mechanically robust, and providing high

thermal conductivity for heat dissipation. The high Q cavity enables VCSEL operation even with a single QD active layer. The cavity takes advantage of the QDs' feature of forming self-buried heterostructures to eliminate optical absorption outside the active region, and simultaneously enables lithographic scaling of the QD active material to control QD number in the active region itself.

4.2 All-Epitaxial Quantum Dot Microcavities

Molecular beam epitaxy is used to grow the QD microcavity illustrated in figure 4.1(a). An initial growth includes a lower 30-pair AlAs/GaAs quarter-wave mirror followed by the first half of a cavity spacer containing a single QD layer active region. The first half of the cavity spacer includes a 1418 Å thick GaAs cavity spacer layer, a 150 Å thick $Al_{0.25}Ga_{0.75}As$ etch stop layer, a 100 Å thick GaAs layer, a single QD layer of density ~3 x 10^{10} cm^{-2} formed from deposition of 2.4 monolayers of InAs, and covered with 350 Å of additional GaAs. The initial growth is finished with a 200 Å sacrificial $Al_{0.7}Ga_{0.3}As$ layer, and finally a 200 Å sacrificial GaAs layer. The sacrificial layers are used as etch masks to define relatively dense arrays of mesas ranging (due to masking and undercutting) from 9 μm down to 0.5 μm diameter. The microcavities contain InAs QDs that range in number from ~ 20,000 for the larger 9 μm mesas to ~50 QDs for the smallest 0.5 μm diameter. An optical photograph looking down on such a QD microcavity array with moderate mesa sizes of ~ 4 μm is shown in figure 4.1 (b). After defining the

QD-containing mesas and removing the GaAs and $Al_{0.7}Ga_{0.3}As$ sacrificial layers, an epitaxial overgrowth that includes the upper part of the cavity spacer of 1312 Å thick GaAs and two upper AlAs/GaAs distributed Bragg reflector pairs complete the QD microcavities. The total thickness of this second growth corresponds to a deposition of 0.35 μm. The two-pair upper mirror forms a relatively low-*Q* microcavity that can provide high-efficiency surface emission, and enables study of the overgrowth and its impact on the QD microcavity and emission efficiency through the Purcell effect.

Figure 4.1 (c) shows atomic force microscope images of completed individual ~ 4 μm diameter (left) and ~0.5 μm diameter (right) QD mesa microcavities. The overgrowth exhibits a relatively strong crystallographic dependence that becomes pronounced for the smaller mesa, but which retains a smooth crystal surface to create the elliptical "lens" shape, especially clear in the smaller cavity. The shorter lateral dimension of the cavity formed by overgrowth of the 0.5 μm mesa (on the right) is ~ 0.8 μm, while the longer dimension corresponds to ~ 3 μm. The height of the microcavity is 440 Å and is close to the height of the starting mesa. Photoluminescence (PL) is studied from the arrays for various temperatures to determine the cavity influence on QD emission. The larger diameter cavities are designed for resonance between the QDs and the cavity at a temperature of ~100 K,

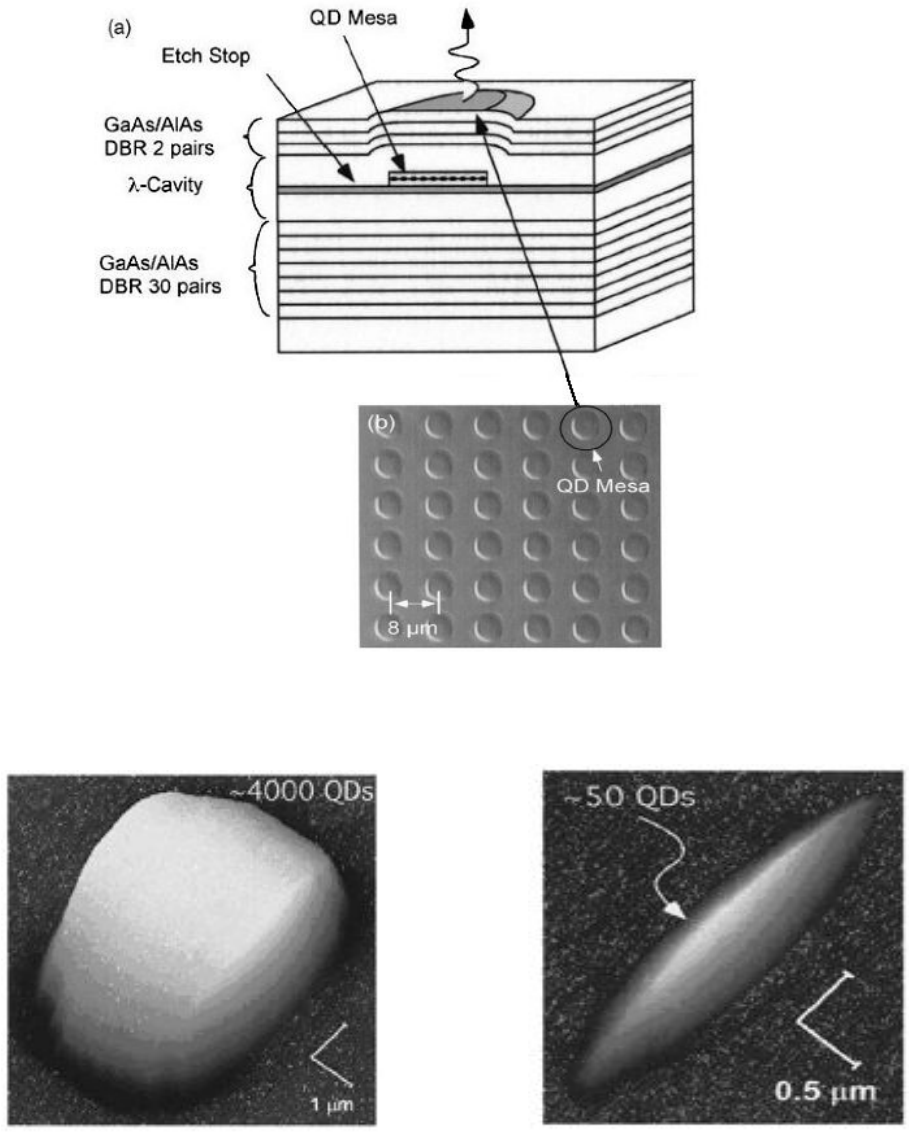

Figure 4.1: (a) Schematic illustration of the QD microcavity based on epitaxial overgrowth of the QD containing mesa. (b) Optical photograph of the 4 μm QD mesa array. (c) Atomic force microscope image of the 4 μm diameter mesa (left) and 0.5 μm mesa (right) following overgrowth.

but cavity wavelength also depends on the lateral mode confinement. Therefore, the difference in temperature dependence of approximately a factor of 10 between the spectral shift in cavity resonance and the spectral shift of the QD transition (set by the material energy gap) is used to determine the precise resonance temperature. Figure 4.2 shows the emission spectra measured for different temperatures for the 4 μm mesa array. Starting from the lowest temperature of 77 K, the emission intensity increases with increasing temperature up to 100 K due to spectral tuning between the cavity resonance and QD transition. At ~100 K the intensity peaks, and then decreases for increasing temperatures. Similar spectral measurements are performed for 9, 8, 7, 6, 5, 4, and 0.5 μm mesa diameter microcavity arrays to determine both the cavity resonance wavelength and the relative emission intensities versus the QD mesa size. The emission data for the different microcavities as set by the QD mesa size are plotted in figure 4.3. The data show a consistent trend of the cavity resonance wavelength blue shifting with decreasing mesa size, a well-known effect due to the lateral optical boundary condition in the microcavity. This trend continues even for the smallest submicron QD mesa diameter of 0.5 μm for the microcavity shown in figure 4.1 (b), demonstrating significant optical confinement even for small microcavity sizes. For these cavities, the lifetime change is given approximately by $\tau_{sp,cav}^{-1}$ is the cavity-enhanced spontaneous

emission rate, $\tau_{sp,bulk}^{-1}$ is the emitter's spontaneous emission rate in bulk semiconductor, c is the speed of light in vacuum, n is the semiconductor refractive index, γ_d is the Lorentzian spectral width due to dipole dephasing, ω_c/Q is the cavity loss rate with ω_c the cavity resonant frequency, w is the lateral optical mode diameter for a lowest-order Bessel function, L is the effective confinement length of the mode, and $f(\mathbf{r}_d)$ is a normalized field strength in the microcavity at the emitter's position, which takes a maximum value of unity as assumed in the last expression on the right in Eq. (4.1).

$$\tau_{\mathrm{sp,cav}}^{-1} = \frac{8(c/n)^3 |f(\mathbf{r}_d)|^2}{w^2 L \omega_c^2 (\gamma_d + \omega_c/Q)} \tau_{\mathrm{sp,bulk}}^{-1} \cong \frac{Q(\lambda_o/n)^3}{\pi^3 w^2 L} \tau_{\mathrm{sp,bulk}}^{-1}, \tag{4.1}$$

The cavity frequency ω_c tracks the lateral mode size w approximately as

$$\omega_c(w) = \left[4.81c^2/(nw)^2 + \omega_c^2(w \to \infty)\right]^{1/2} \tag{4.2}$$

where n is the refractive index of the semiconductor (assuming a Bessel function), so that a blue-shift in the cavity frequency occurs with a decrease in mode size. Inserting the mode size dependence on frequency of Eq. (4.2) into Eq. (4.1), we can relate the cavity enhancement to the lateral mode size through the spectral shift it induces, given by $\tau_{sp,cav}^{-1} / \tau_{sp,bulk}^{-1} = 0.26[Q\lambda_o/(nL)][1 - \omega_c^2(w \to \infty)/\omega_c^2(w)]$

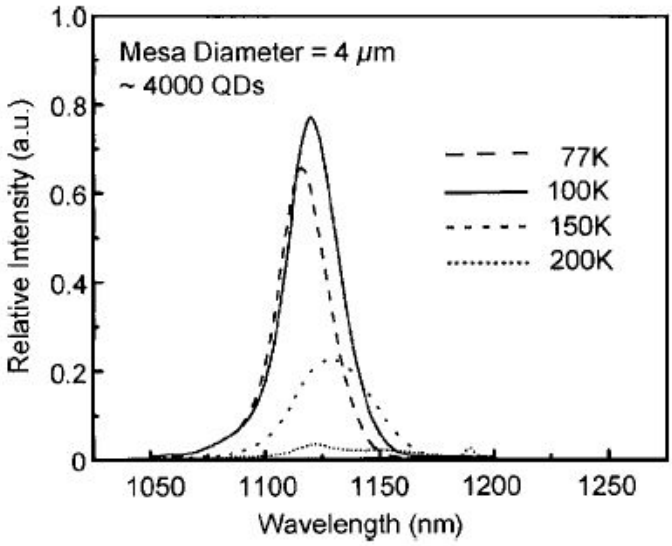

Figure 4.2: Spectral emission of the 4 μm QD mesa microcavity for various temperatures. Resonance is obtained at 100 K.

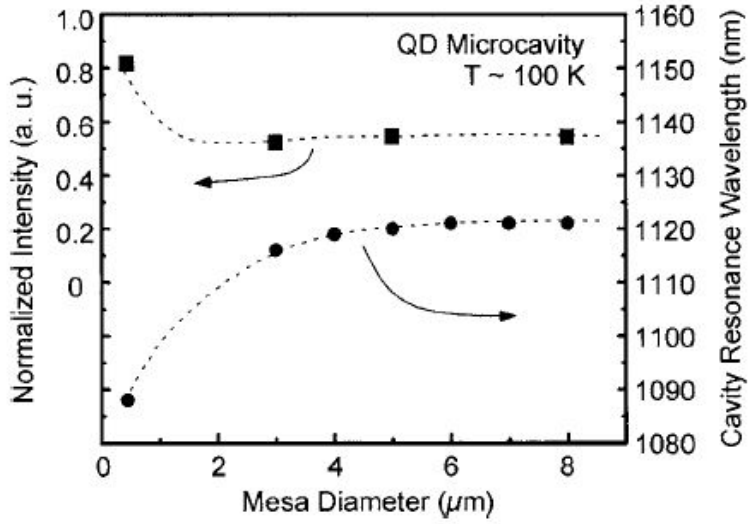

Figure 4.3: Plots of relative efficiency and resonant wavelength of the microcavity versus different sizes of the QD containing mesa.

The Purcell effect ideally produces an increase in integrated intensity with reduction of cavity size when the cavity mode coupling strength exceeds the collective coupling due to all other weakly confined optical modes that may interact with the QDs [23].

In oxide-apertured microcavities this occurs when the lateral cavity size is less than ~ 1 μm [22]. In the present study the relative integrated intensity is found using a similar spot size to excite each mesa array, and then normalizing the integrated intensity by the QD mesa fill factor in the array as excited by the pump spot. The upper data in figure 4.3 show that the integrated QD emission is constant from the 9 μm down to the 4 μm mesa size, but increases for the smallest 0.5 μm mesa. The increase in efficiency observed for the array of 0.5 μm mesa QD microcavities compared with the larger sizes is ~ 50%. The Q values of the cavities are measured to be ~50, while the effective cavity length can be estimated from the field penetration into the semiconductor mirrors as $L = 1.5\lambda_o / n$. Therefore the emission into the 0.5 μm QD mesa cavity can also be estimated from the blueshifted frequency as also increasing by $\tau_{sp,cav}^{-1} / \tau_{sp,bulk}^{-1} \approx 0.5$.

This increase in intensity for the smallest cavity, taken with the continued blue shift of the emission wavelength with reducing microcavity size, is a clear indication of the Purcell effect and a major benefit of the microcavity even for low Q values. Therefore both the blue shift in the resonance wavelength and the integrated intensity dependence track the lateral size dependence expected due to

microcavity confinement. Considering the cavity shape formed by the epitaxial overgrowth over the smallest 0.5 μm mesa sizes, it is significant that cavity confinement is still achieved. The smooth growth is important for low optical scattering, while the curved shape can lead to increased collection angle of the spontaneous emission and lateral reduction of the mode volume. It is reasonable to expect that the actual cavity shape can be controlled by mesa height (which is ~ 450 Å in the present experiment), and can therefore ultimately be engineered to control the cavity characteristics. Shallower mesas will produce less curvature in the overgrowth, and may be more useful for very high-Q microcavities. Taller mesas such as used here that can give a substantial lens shape may be more useful for lower-Q microcavities, but stronger lateral confinement.

Finally, we consider what cavity Q is required to maximize the Purcell effect for a single QD spontaneous light source that can operate with maximum thermoelectric cooling for an operating temperature of ~150 K. The needed Q is set by the QD's homogeneous linewidth, which from experimental measurements is on the order of ~ 3 meV at 150 K [54]. The needed cavity Q at 1.1 μm is therefore moderate (~350), and can be achieved by engineering the mesa height and increasing the upper mirror pair number. The Qs measured in the present microcavities are ~ 50, set by the two-pair upper mirror, and can be increased with a few additional upper mirror pairs.

4.3 Buried Heterostructure QD VCSEL

Based on the results of section 4.2, another crystal was grown which is similar to the microcavity structure, but with 30 pairs of upper DBR to increase the cavity Q. Optical confinement is provided vertically by the mirrors pairs. Lateral optical confinement is through the mismatched cavity height at the mesa edge.

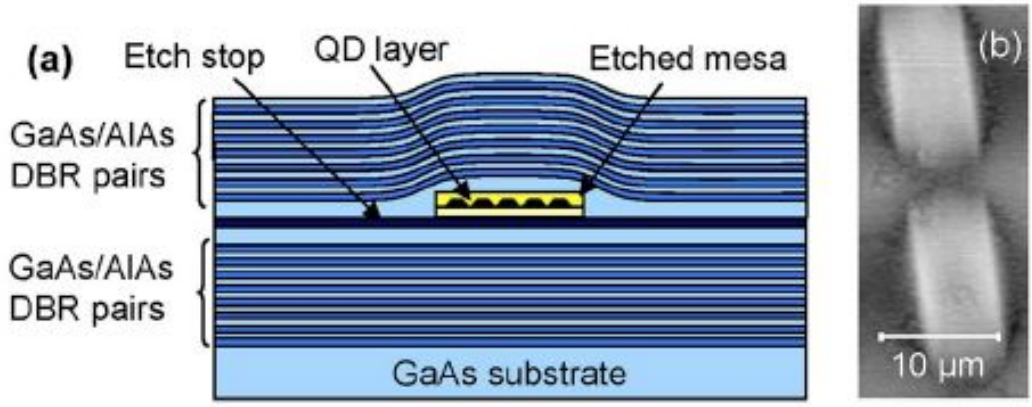

Figure 4.4: (a) Schematic of the microcavity VCSEL structure. (b) AFM image of the buried structure.

Because vertical reflectors exist both inside and outside the mesa (figure 4.4 a), lateral mode confinement comes from the vertical resonance shift of the cavity mode due to the mesa as discussed in chapter 2. Atomic force microscope images, such as shown in figure. 4.4 (b) for an array of 6.1 μm mesas, reveal that the overgrown structure is actually highly asymmetric due to preferential growth along one direction, and results in lens-like shapes.

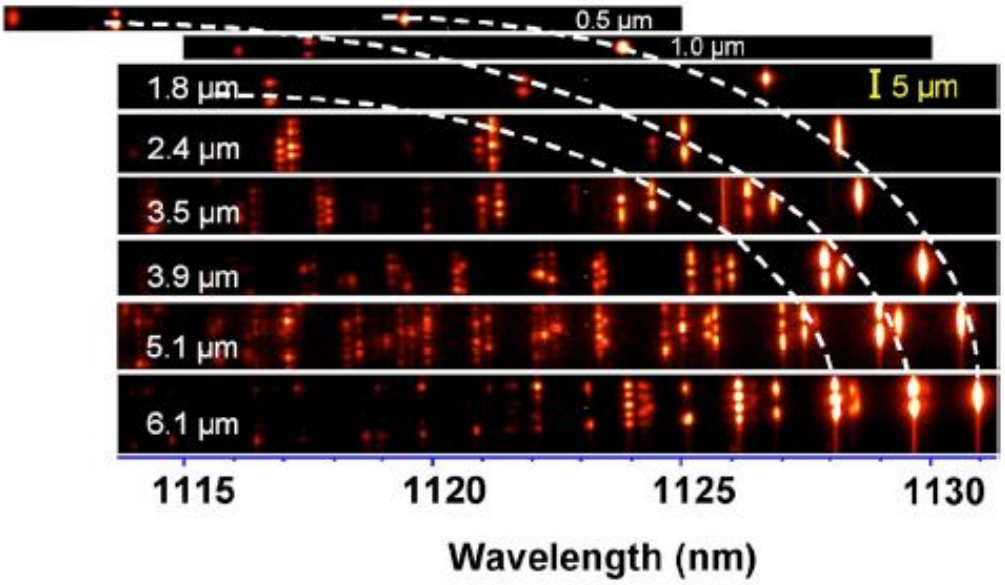

Figure 4.5: Modal characteristics of the cavities at T=35 K. The spatially (position along slit) and spectrally resolved PL from individual cavities is displayed for various mesa diameters.

The emissions from individual cavities are studied using a pulsed Ti:sapphire laser (pulsewidth ~ 5 ps) that excite the QDs through electron-hole generation above the GaAs band edge. The sample is maintained at low temperature in a helium flow cryostat during measurement. The PL signal is collected with a 0.5 numerical aperture (NA) objective, dispersed by a 0.5 m spectrograph, and imaged onto a two-dimensional charge coupled device array detector [55]. Figure 4.5 shows the spectral images, i.e., PL intensity as a function of wavelength and position along the slit, of individual cavities based on mesas with diameter, D, ranging from 6.1 to 0.5 μm. The images reveal a rich mode

structure, with mode spacing between transverse modes clearly increasing strongly with decreasing mesa size. The latter, together with the blue shift of the cavity resonances, reflects the lateral optical confinement even for small mesa sizes [56,57]. The individual modes are spectrally well resolved and can also be visualized by performing spectrally resolved mode mapping [58]. They closely resemble the $LP_{n,m}$ modes of a cylindrical stepped-index dielectric cavity with a (weak) effective index step at the mesa edge. Each mode is further split into linearly polarized doublets due to the asymmetric overgrowth. The Q values, obtained from the Lorentzian linewidth of the PL peaks, are further studied for mesas of various sizes. Plotted in figure 4.6 are the Qs of individual cavities with decreasing size, measured at sufficiently low excitation intensity so as to exclude linewidth narrowing effects due to lasing [58]. The values range from $Q \sim 33{,}000$ for the largest cavities with ~ 6 μm mesas down to $Q \sim 10{,}000$ for cavities based on 0.5 μm diameter mesas. Both the raw and deconvoluted values are shown. The deconvoluted value takes into account resolution of the system while calculating the Q. The highest Q values exceed those of a recent report based on three halves wavelength cavity spacers [58]. The high Q combined with high quality QDs are key to obtaining QD VCSELs with a single active layer. Although the Q decreases with mesa size similar to reports for other microcavity systems [58-60], the present measurements indicate that for the smallest mesas that contain only a single QD

[56,57] entering the strong coupling regime [26,27] may be feasible with this all-epitaxial lithographically defined QD microcavity.

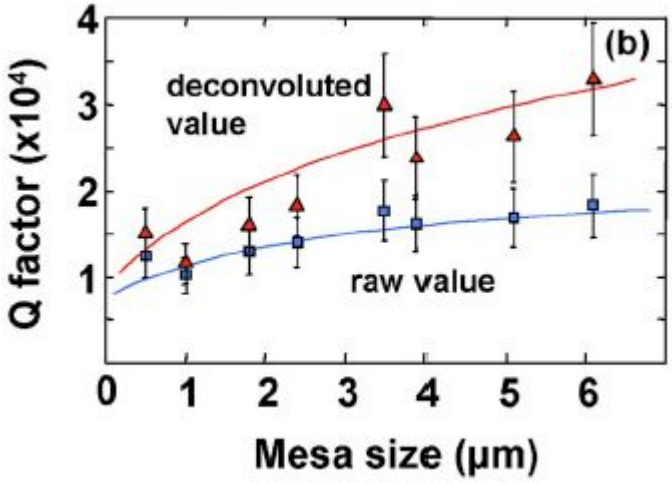

Figure 4.6: Quality factor for different cavity sizes measured at T=35 K. Both the raw data and the deconvoluted data are shown.

The lasing characteristics are studied under experimental conditions similar to the ones described above with the temperature typically maintained at 35 K. Previous studies of etched-pillar [58,59] or oxide-apertured microcavities [61] have not demonstrated lasing, even with multiple QD active layers. The VCSEL operation with a single QD active layer suggests that either the passive Q in the present microcavities is higher, or the QD quality is better, or possibly both. In figure 4.7 (a) the light out versus pump intensity curves for 6.1- and 5.1- μm-diam cavities are shown on linear and log-log plots (inset). The largest powers incident

on the sample are on the order of ~10 mW corresponding to ~5 x 10^8 W peak power, 80 MHz repetition rate, 6 ps pulse width, 780 nm wavelength), while the laser spot is focused to a ~20- μm-diam spot. However, a meaningful value for the actual intensity at the QD location is difficult to estimate due to pump absorption in the large number of overgrown layers, and the intensity scale is therefore left in arbitrary units. As threshold is approached, a pronounced linewidth narrowing is also observed as shown for the D = 6.1 μm cavity in figure 4.7 (b). The linewidth decreases to values close to the spectrometer resolution (~50 μeV) and a weak increase is observed at the highest pump powers, most likely due to heating effects. The spectral features below and above threshold are shown in figure 4.7 (c). The laser emission, which is highly linearly polarized, generally occurs at the fundamental mode only. However, some cavities in the array also lase on higher order modes, and multimode lasing has been observed at temperatures exceeding

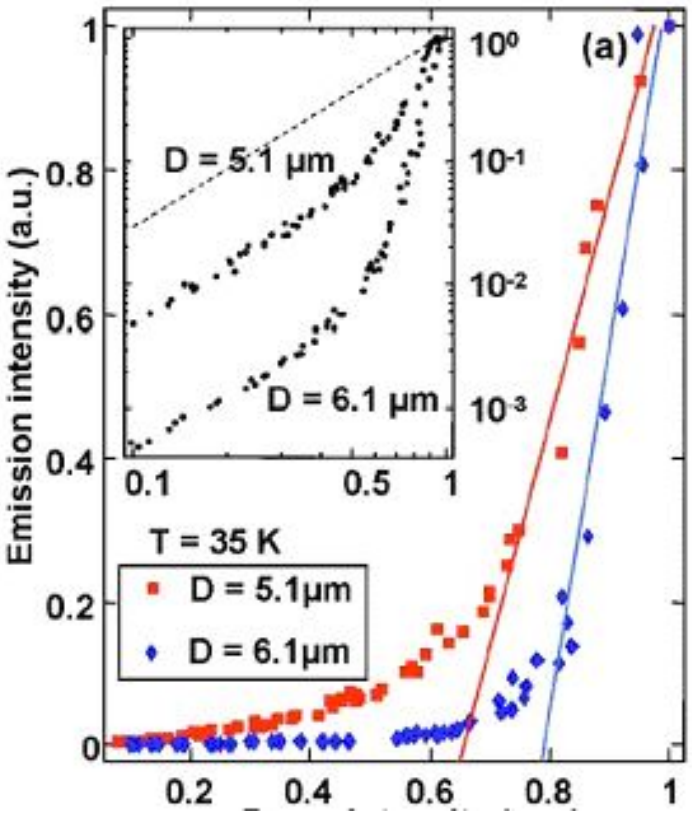
(a)
Emission intensity (a.u.)
D = 5.1 μm
D = 6.1 μm
T = 35 K
D = 5.1μm
D = 6.1μm
10⁰
10⁻¹
10⁻²
10⁻³
0.1
0.5
1
0
0.2
0.4
0.6
0.8
1

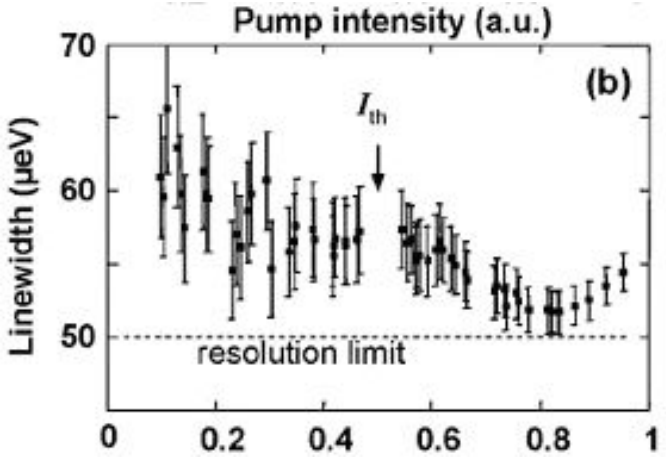
Pump intensity (a.u.)
(b)
Linewidth (μeV)
I_{th}
resolution limit
70
60
50
0
0.2
0.4
0.6
0.8
1

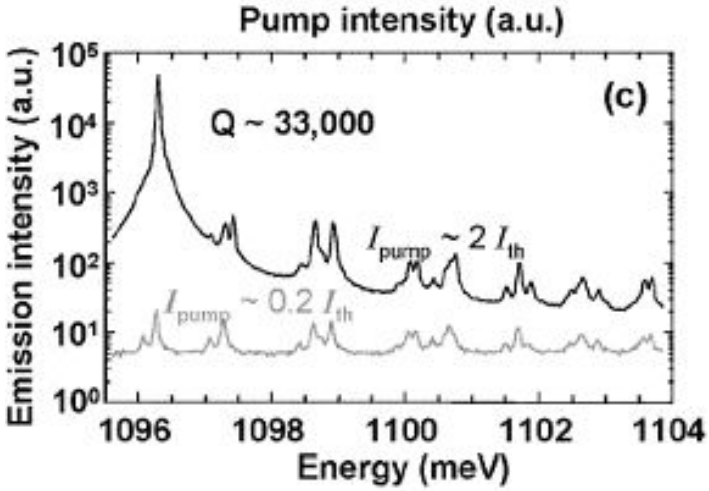

Figure 4.8: (a) Emission vs excitation (L-L) curves for a D=6.1 μm and D=5.1 μm mesa measured at *T*=35 K. The inset shows a log-log plot of the same data. (b) Linewidth of the lasing resonance as a function of pump intensity, extracted using a Lorentzian fit, for the D =6.1 μm cavity in (a). (c) Emission spectrum below and above threshold for the same cavity.

200 K. The modal characteristics of VCSELs are generally set by spectral tuning between the gain peak and cavity resonances, and multimode lasing at higher temperatures may be due to the higher gain excited state lasing in the QD active region. The threshold and lasing characteristics change with temperature is expected due to the spectral overlap between the inhomogeneously broadened gain profile of the QDs and the cavity resonances. In agreement with the targeted spectral match around ~ 100 K, the lasing threshold first decreases in the temperature range from 5 to 100 K and then increases for temperatures greater than 100 K.

In summary, a new type of all-epitaxial microcavity is demonstrated that forms a buried heterostructure QD VCSEL. Quality factors as large as 33000 have been measured, with ground state laser operation achieved using only a single QD active layer. As an all-epitaxial structure, the device is mechanically robust, provides high thermal conductivity and with a modified approach provides a potential for electrical injection. Its lithographic definition is an important step in manufacturing, and makes it highly attractive for single QD cavity quantum electrodynamics experiments where both high-Q and small mode volumes are desirable.

CHAPTER 5

SUMMARY

The focus of this dissertation has been to implement an epitaxial regrowth based fabrication process for vertical cavity lasers. Using this approach it is possible to incorporate photonic patterns within the optical cavity of laser diodes to provide full control of the modal overlap with the optical gain. Patterns of interest are two dimensional circular gratings, photonic crystal, or any other random patterns to engineer the transverse mode profile. Lithographic patterning allows excellent uniformity and flexibility of pattern design, and the all-epitaxial devices have better reliability and thermal impedance.

The design of a GaAs based all-epitaxial grating confined VCSEL has been studied and realized experimentally. Lateral mode confinement in the VCSEL is obtained due to the epitaxial crystal step formed by shallow circular grating mesas that creates a resonant shift for the vertical component of the optical mode. An epitaxial regrowth of semiconductor mirrors over the gratings simultaneously confines the mode in the vertical and lateral directions. The grating uses selective Fermi-level pinning at a hetero-interface to confine the current to the same regions as the optical mode. An increase of efficiency is obtained in side-by-side comparison with devices that lack the grating. The far-field radiation pattern which is indicative of the coherent near-field spot size is larger compared to a device

without grating. This proves that there is coupling of gain and optical mode around the grating rings and also that the mode is confined within the rings of the circular grating. The present design demonstrates the potential to engineer high performance VCSELs through simultaneous control of mode and gain profiles. However, this device could be improved by optimizing the ring sizes and spacing by matching the rings to the peaks of the first order Bessel function. Current injection efficiency can be increased by making the outer rings smaller compared to the inner rings by using a chirped grating, since the mode intensity is peaked at the center. There could also be variations in current confinement schemes and improvements in epitaxial regrowth that would reduce scattering loss at the interface and improve device performance significantly.

Using a similar regrowth technique, a laser diode incorporating a buried etched void photonic pattern consisting of air-GaAs has also been demonstrated in this work. High index contrast 2-D photonic crystal patterns that are placed close to the active region have a significant impact on the propagation characteristics of the optical mode. Side-by-side comparison with devices without any photonic pattern shows lower threshold current densities and higher slope efficiencies in the devices with the etched-void photonic pattern. The spectral characteristics indicates that it has fewer Fabry-Perot modes compared to the devices without the pattern, and shows that the etched-void photonic pattern improves modal selectivity through Bragg reflection. This fabrication process can be extended to obtain coherent large

area surface emission since certain designs of photonic patterns can diffract light in the vertical direction. Photonic crystal based VCSELs can also be fabricated with this approach.

The new technology has also been applied to QD devices to obtain all-epitaxial microcavities and high Q microcavity VCSELs which can be useful as single photon sources. A new type of VCSEL has been demonstrated that uses a lithographically defined intracavity mesa to confine the optical mode as well as isolate the QDs to the same region of the microcavity. Very high Q cavities were obtained, and ground state lasing was demonstrated with only a single quantum dot active layer. A significant improvement of the Purcell effect has been observed for spontaneous light sources. Even though these devices were optically pumped, the design of these structures allows electrical injection very easily due to relatively thick epitaxial layers on top of the microcavities. For example, Fermi-level pinning that was discussed to provide current confinement in the grating VCSEL can be easily implemented. This can provide monolithic integration for applications such as quantum computing and quantum cryptography.

In conclusion, this research demonstrates that epitaxial regrowth based process for vertical cavity laser diodes is a promising approach to engineer high performance lasers that can lead to improvement in the transverse overlap between the optical mode and gain to provide increased single-mode selectivity, lower

threshold, and improve the device efficiency. It is also highly attractive for fabricating manufacturable quantum light sources.

References

[1] K. Iga, F. Koyama, and S. Kinoshita, IEEE J. Quantum Electron. **24**, 1845 (1988)

[2] J. L. Jewell, J. P. Harbison, A. Scherer, Y. H. Lee, and L. T. Florez, IEEE J. Quantum Electron. **27**, 1332 (1991)

[3] D. G. Deppe, D. L. Huffaker, C. C. Lin, and T. J. Rogers, *Conference on Lasers and Electro-Optics 1994 Technical Digest Series*, Anaheim, CA, 8–13 May 1994, Vol. 8, CPD2-1/3-6/8

[4] J. L. Jewell, A. Scherer, S.L. McCall, Y. H. Lee, S. Walker, J. P. Harbison, and L.T. Florez, Electron. Lett. **25,** 1123 (1989)

[5] B. Tell, Y. H. Lee, K.F. Brown-Goebeler, J. L. Jewell, R.E. Leibenguth, M.T. Asom, G. Livescu, L. Luther, and V. D. Mattera, Appl. Phys. Lett., **57**, 1855 (1990)

[6] J. M. Dallessasse, N. Holonyak, Jr., A.R. Sugg, T. A. Richard, and El-Zein, Appl. Phys. Lett. **57**, 2844 (1990)

[7] K. D. Choquette, M. Hong, R. S. Freund, J. P. Mannaerts, R. Wetzel, and R. Leibenguth, IEEE Photonics Technol. Lett. **5**, 284 (1993)

[8] L. Chirovsky, W. Hobson., R. Leibenguth, S. Hui, J. Lopata G. Zydik, G. Giaretta, K. Goosen, J. Wynn, A. Krishnamoorthy, B. Tseng, J. Vandenberg, and L. D'Asaro, IEEE Photonics Technol. Lett., 11, 500 (1999)

[9] M. Ortsiefer, R. Shau, G. Bohm, F. Kohler, and M. C. Amann, Appl. Phys. Lett., **76,** 2179 (2000)

[10] G. M. Yang, M. H. MacDougal, and P. D. Dapkus, Electron. Lett. **31**, 886 (1995)

[11] D. L. Huffaker and D. G. Deppe, IEEE Photonics Technol. Lett. **11**, 934 (1999)

[12] K. L. Lear, A. Mar, K. D. Choquette, S. P. Kilcoyne, R. P. Schneider, and K. M. Geib, Electron. Lett. **32**, 457 (1996)

[13] R. Jager, M. Grabherr, C. Jung, R. Michalzik, G. Reiner, B. Weigl, and K. J. Ebeling, Electron. Lett. **33**, 974 (1997)

[14] D. Lu, J. Ahn, H. Huang, and D. G. Deppe, Appl. Phys. Lett. **85**, 2169 (2004)

[15] D.S. Song, S.H. Kim, H.G. Park, C.K. Kim, and Y.H. Lee, Appl. Phys. Lett. 80, 3901 (2002)

[16] N. Yokouchi, A.J. Danner, K.D. Choquette, "Vertical-cavity surface-emitting laser operating with photonic crystal seven-point defect structure," Appl. Phys. Lett. 82, 3608 (2003)

[17] O. Painter, R.K. Lee, A. Scherer, A. Yariv, J.D. O'Brien, P.D. Dapkus, and I. Kim, Science 284, 1819 (1999)

[18] Y. Arakawa and H. Sakaki, *Appl. Phys. Lett.*, **40** 939 (1982)

[19] Y. Arakawa and A. Yariv, *IEEE J. Quantum Electron.* **22** 1887 (1986)

[20] E. M. Purcell, Phys. Rev. **69**, 681 (1946)

[21] L. A. Graham, D. L. Huffaker, Q. Deng, and D. G. Deppe, Appl. Phys. Lett. **72**, 1670 (1998)

[22] J. M. Gerard, B. Sermage, B. Gayral, B. Legrand, E. Costard, and V. Thierry-Mieg, Phys. Rev. Lett. **81**, 1110 (1998)

[23] L. A. Graham, D. L. Huffaker, and D. G. Deppe, Appl. Phys. Lett. **74**, 2408 (1999)

[24] T. Yoshie, J. Vuckovic, A. Scherer, H. Chen, and D. G. Deppe, Appl. Phys. Lett. **79**, 4289 (2001)

[25] T. D. Happ, I. I. Tartakovskii, V. D. Kulakovski, J.-P. Reithmaier, M. Kamp, and A. Forchel, Phys. Rev. B **66**, 041303 (2002)

[26] T. Yoshie, A. Scherer, J. Hendrickson, G. Khitrova, H. M. Gibbs, G. Rupper, C. Ell, O. B. Shchekin, and D. G. Deppe, Nature (London) **432**, 200 (2004)

[27] J. P. Reithmaier, G. Sek, A. Loffler, C. Hofmann, S. Kuhn, S. Reitzenstein, L. V. Keldysh, V. C. Kulakovski, T. L. Reinecke, and A. Forchel, Nature (London) **432**, 197 (2004)

[28] Z. Zou, D. L. Huffaker, S. Csutak, and D. G. Deppe, Appl. Phys. Lett. **75**, 22 (1999)

[29] T. Yoshie, O. B. Shchekin, H. Chen, D. G. Deppe, and A. Scherer, Electron. Lett. **38**, 799 (2002)

[30] T. Yang, O. Shchekin, J. D. O'Brien, and D. G. Deppe, Electron. Lett. **39**, 1657 (2003)

[31] D. Lu, J. Ahn, H. Huang, and D. G. Deppe, Appl. Phys. Lett. **85**, 2169 (2004)

[32] J. Ahn, D. Lu, and D. G. Deppe, Appl. Phys. Lett. **86**, 021106 (2005)

[33] G.R. Hadley, Opt. Lett. 20, 1483 (1995)

[34] D.G. Deppe, T.-H. Oh, and D.L. Huffaker, IEEE Phot. Tech. Lett. 9, 713 (1997).

[35] T.Oh, Ph.D. Dissertation, 1999

[36] J. Kim, D. Lim, and G. Yanga, J. Vac. Sci. Technol. B 16.2., 558 (1998)

[37] A. Cho, J. Vac. Sci. Tech., vol. 8, pp. S31, 1971.

[38] C. T. Forxon, and B. A. Joyce, Surface Sci., vol. 50, pp. 434 (1975)

[39] T.-H. Oh, M. R. McDaniel, D. L. Huffaker, and D. G. Deppe, IEEE Photon. Technol. Lett., vol. 10, 12 (1998)

[40] H. P. Meier, E. Van Gieson, P. W. Epperlein, C. Harder, and W. Walter, *J. Cryst. Growth,* vol. 95, pp. 66–70 (1989)

[41] E. Bockenhoff and H. Benisty, *J. Cryst. Growth,* vol. 114, pp. 619–632 (1991)

[42] M. Walther, T. Rohr, G. Bohm, G. Trankle, and G. Weimann, *J. Cryst. Growth,* vol. 127, pp. 1045–1050 (1993)

[43] D.Gazula, J. Ahn, D. Lu, H. Huang, and D. G. Deppe, Appl. Phys. Lett. 86, 161117 (2005)

[44] D. Ohnishi, K. Sakai, M. Imada, and S. Noda, Electron. Lett. 39, 612 (2003)

[45] M. Meier, A. Mekis, A. Dodabalapur, A. Timko, R. E. Slusher, J. D. Joannopoulos, O. Nalamasu, Appl. Phys. Lett. 74, 7 (1999)

[46] M. Notomi, H. Suzuki, and T. Tamamura, Appl. Phys. Lett. 78, 1325 (2001)

[47] M. Imada, S. Noda, A. Chutinan, T. Tokuda, M. Murata, and G. Sasaki, Appl. Phys. Lett. 75, 316 (1999)

[48] S. Noda, M. Yokoyama, M. Imada, A. Chutinan, M. Mochizuki, Science 293, 1123 (2001)

[49] H.-Y. Ryu, S.-HY. Kwon, Y.-J. Lee, Y.H. Lee, and J.-S. Kim, Appl. Phys. Lett. 80, 3476 (2002).

[50] M. Berggen, A. Dodabalapur, R.E. Slusher, Z. Bao, A. Timko, and O. Nalamasu, Electron. Lett. 34, 90 (1998)

[51] D. Gazula, S. Quadery, and D.G. Deppe, Elect. Lett, 41, 1223 (2005)

[52] K. M. Ho, C. T. Chan, and C. M. Soukoulis, Phys. Rev. Lett. 65, 3152–3155 (1990)

[53] R. D. Meade, A. M. Rappe, K. D. Brommer, J. D. Joannopoulos, and O. L. Alerhand, Phys. Rev. B **48**, no. 11, pp. 8434-8437 (1993)

[54] P. Borri, W. Langbein, S. Schneider, U. Woggon, R. L. Sellin, D. Ouyang, and D. Bimberg, IEEE J. Quantum Electron. **8**, 984 (2002)

[55] H. Htoon, H. B. Yu, D. Kulik, J. W. Keto, O. Baklenov, A. L. Holmes, B. G. Streetman, and C. K. Shih, Phys. Rev. B **60**, 11026 (1999)

[56] A. Muller, C. K. Shih, J. Ahn, D. Lu, and D. G. Deppe, Opt. Lett. (ess_.)

[57] D. Lu, J. Ahn, S. Freisem, D. Gazula, and D. G. Deppe, Appl. Phys. Lett. **87**, 163105 (2005)

[58] D. Sanvitto, A. Daraei, A. Tahraoui, M. Hopkinson, P. W. Fry, D. M. Whittaker, and M. S. Skolnick, Appl. Phys. Lett. **86**, 191109 (2005)

[59] A. Loffler, J. P. Reithmaier, G. Seak, C. Hofmann, S. Reitzenstein, M. Kamp, and A. Forchel, Appl. Phys. Lett. **86**, 111105 (2005)

[60] T. Rivera, J. -P. Debray, J. M. Gerard, B. Legrand, L. Manin-Ferlazzo, and J. L. Oudar, Appl. Phys. Lett. **74**, 911 (1999)

[61] N. G. Stoltz, M. Rakher, S. Strauf, A. Badolato, D. D. Lofgreen, P. M. Petroff, L. A. Coldren, and D. Bouwmeester, Appl. Phys. Lett. **87**, 013105 (2005)

Vita

Deepa Gazula was born in Bodhan, India on March 28, 1978, the daughter of Helen Sumitra Mani and David Krupadanam. She received her Bachelors degree in Metallurgical Engineering from Indian Institute of Technology, Madras in June 1999. She entered the graduate school in Rochester Institute of Technology, Rochester, NY and obtained the Master of Science degree in Material Science and Engineering in 2001. During 2001-02, she worked as a Staff Engineer at IBM Microelectronics in Fishkill, NY and participated in the development of 193 nm lithography technology. In 2002, she joined the Ph.D. program in the Department of Electrical and Computer engineering at The University of Texas at Austin.

Permanent address: 12-13-677/83, Kimtee Colony, Tarnaka, Hyderabad, India, 500017.

This dissertation was typed by the author.